Available online at www.sciencedirect.com
ScienceDirect
Journal of Sound and Vibration 315 (2008) 118–145
JOURNAL OF SOUND AND VIBRATION
www.elsevier.com/locate/jsvi

An efficient quadrilateral element based on improved zigzag theory for dynamic analysis of hybrid plates with electroded piezoelectric actuators and sensors

S. Kapuria*, S.D. Kulkarni

Department of Applied Mechanics, Indian Institute of Technology Delhi, Hauz Khas, New Delhi 110016, India

Received 23 August 2007; received in revised form 21 December 2007; accepted 19 January 2008
Handling Editor: L.G. Tham
Available online 3 March 2008

Abstract

An efficient four-node quadrilateral element is developed using a coupled improved zigzag theory for the dynamic analysis of hybrid plates with segmented piezoelectric sensors and actuators. The theory considers a third-order zigzag approximation for inplane displacements, a layerwise quadratic approximation for the electric potential and a layerwise variation of the deflection to account for the piezoelectric transverse normal strain. The conditions on transverse shear stresses at the interfaces and at the top and bottom are satisfied exactly in the presence of electric loading. In a novel concept, the degrees of freedom (dof) corresponding to the quadratic component of the electric potential distribution are associated with the physical nodes and the electric potentials of the electroded piezoelectric surfaces are attached to separate electric nodes. The requirement of C^1 continuity of interpolation functions of the deflection is circumvented by employing an improved discrete Kirchhoff constraint technique. Comparison of the present results for natural frequencies and mode shapes for a variety of bimorph, hybrid composite and sandwich plates, with three-dimensional (3D) analytical and FE solutions, and those of other available elements establishes the superiority of the present element with respect to accuracy, robustness and computational efficiency. The comparison also establishes the superiority of the zigzag theory over the smeared third-order theory having the same number of dof.

1. Introduction

Hybrid composite and sandwich plates with some distributed, surface-bonded and/or embedded piezoelectric sensors and actuators are now widely used in active vibration, acoustic, shape and position control applications. The piezoelectric sensors/actuators are always electroded with a metallic coating, which makes their surfaces equipotential. It is revealed from the review papers [1,2] on finite element (FE) modelling of piezoelectric hybrid laminates that most of the finite elements consider electric potential degrees of freedom (dof) as nodal variables, and some [3–8] treat them as elemental variables making them constant along inplane directions over an element. In the latter case, the inplane electric fields which may be induced due to a direct

*Corresponding author. Tel.: +91 11 26591218; fax: +91 11 26581119.
E-mail address: kapuria@am.iitd.ac.in (S. Kapuria).

0022-460X/$ - see front matter © 2008 Elsevier Ltd. All rights reserved.
doi:10.1016/j.jsv.2008.01.053

piezoelectric effect cannot be accounted for. In both cases, to model the equipotential condition on the electroded surfaces, it would be necessary to impose the constraints of equality on the electric dof of the nodes/elements on the same electroded surface or to average them as an approximation [8,9], both of which are tedious tasks. Sze and Yao [10] presented a solid element wherein the electric potential is considered linear across the piezoelectric layer and the electric dof corresponding to a piezoelectric patch are attached to a separate electric node instead of the physical nodes. But this approach cannot account for the inplane electric fields, as all the electric dof are associated with electric nodes.

Three-dimensional (3D) finite elements [10–13] for dynamic analysis of piezoelectric laminates result in a very large problem size which becomes computationally intractable. Hence, efficient and accurate two-dimensional (2D) theories, and their simple and robust FE models are needed. Coupled discrete layer theories (DLTs) [14,15] considering layerwise linear variation of inplane displacements and electric potential yield accurate results, but they too suffer from an excessive number of dof in proportion to the number of layers. To improve the computational efficiency, FE models based on the mixed field 2D theories have been proposed, which consider a global equivalent single layer (ESL) approximation for the mechanical field variables and a layerwise approximation for the electric potential. Four-node [3,4,16], eight-node serendipity [5,17,18] and nine-node Lagrange [6,19] isoparametric elements have been developed for dynamics of hybrid plates and shells, using the first-order shear deformation theory (FSDT), which requires only C^0 continuity of the displacement variables. Gu et al. [20] developed a four-node nonconforming rectangular element with 7 mechanical dof per node, based on the refined third-order theory (TOT) of Reddy [21], which requires C^1 continuity of deflection along the element boundary. Nine-node [22] plate elements with 11 mechanical dof per node and an eight-node degenerate shell element [7] with 9 dof per node have been developed based on higher order theories (HOTs), requiring C^0 continuity of the deflection. The ESL theories are economical but they do not account for the layerwise (zigzag) nature of variation of the inplane displacements across the laminate thickness as observed from 3D piezoelasticity solutions [23,24]. Hence, they are inadequate for obtaining an accurate response of moderately thick and even thinner laminates with strong layerwise inhomogeneities.

To retain the merits of the DLTs and economy of the ESL theories, Di Sciuva [25] and Cho and Parmerter [26] presented an efficient layerwise theory also known as zigzag theory (ZIGT), wherein the inplane displacements are assumed to have a layerwise linear variation with a global cubic variation, but the number of displacement variables are reduced to five by imposing the conditions of continuity of transverse shear stresses at the interfaces and shear traction-free conditions at the top and bottom surfaces. A historical review of the available zigzag theories for elastic laminated plates and shells has been presented by Carrera [27]. The ZIGT of Refs. [25,26] was extended to the piezoelectric laminate by the first author and coworkers for hybrid beams [28] and plates [29,30]. This theory requires C^1 continuity of deflection along the inter-element boundary like the TOT, which poses difficulties in developing simple conforming quadrilateral elements, unlike the FSDT and HOTs. Topdar et al. [31] developed a four-node rectangular element with 8 mechanical dof per node employing the third-order ZIGT [26] for dynamics of adaptive plates. Robaldo et al. [32] presented a unified FE formulation for ESL theories and DLT and Reissner-type zigzag theory for dynamic analysis of adaptive plates. In the Reissner-type zigzag theory [32], constitutive equations for shear stresses are satisfied only approximately. Unlike the theories in Refs. [31,32], the coupled improved zigzag theory (IZIGT) of [29] directly accounts for the layerwise variation of transverse displacement caused by the electric field through the d_{33} effect, which is a unique feature of this theory. It also satisfies exactly the conditions on the transverse shear stresses at the layer interfaces and the top and bottom surfaces, in the presence of an inplane electric field that may be induced by a direct piezoelectric effect.

Exact 3D piezoelasticity solutions reveal [29] that the electric potential ϕ follows a nearly quadratic variation across piezoelectric layers and the assumption of a linear variation for ϕ can cause a significant error in the computed response [8,33]. While most of the above literatures consider a linear variation of ϕ across the layer, a sublayerwise linear variation is considered in Refs. [17,28–30], in which the piezoelectric can be divided into an arbitrary number of sublayers. Such a description can yield a fairly accurate prediction of ϕ [29], but it results in a large number of unknown potentials and may still give erroneous results for the transverse electric displacement and inplane normal stresses in the piezoelectric layers. Higher order approximations of the electric potential have been adopted by Rogacheva [34] for single-layer piezoelectrics and by Krommer [35],

and Vasques and Rodrigues [8] for layered smart beams, wherein approximations are made on the axial component of the electric field or the electric displacement.

In this work, an efficient four-node quadrilateral element is developed for dynamic analysis of hybrid plates based on the improved third-order zigzag theory [30]. The electric potential is approximated to follow a quadratic variation across the piezoelectric layers, as observed from the exact 3D piezoelasticity solution [29]. The transverse displacement is approximated by superposing an explicit layerwise contribution of the transverse electric field on a constant term. The requirement of C^1 continuity of the interpolation functions of the deflection is circumvented by using the improved discrete Kirchhoff quadrilateral (IDKQ) functions, as applied successfully by the authors [36] for elastic multilayered plates. The element has four physical nodes with seven kinetic dof per node. In a novel concept, the electric potential dof associated with an equipotential electroded surface are attached to an electric node, which has no physical coordinates unlike the physical nodes, and the electric dof corresponding to the quadratic component of potential distribution are associated with the physical nodes. This conveniently models the equipotential condition of electroded surfaces with a significantly reduced number of electric dof, and also allows for the inplane electric field that may be induced by the direct piezoelectric effect. The element based on an improved TOT accounting for transverse extensibility in the presence of an electric field is also developed as a special case.

2. Coupled zigzag theory approximations

Consider a smart hybrid plate (Fig. 1) made of perfectly bonded layers of angle-ply composite materials with some layers of piezoelectric materials acting as sensors and actuators. The piezoelectric materials considered here exhibit class mm2 symmetry with respect to the principal material axes [37], as observed in the commonly used piezoelectric materials PZT and PVDF. These are poled along the thickness direction z. Due to the presence of piezoelectric patches, the number of layers L and the total thickness h may vary from one segment of the plate to another. The reference xy-plane ($z = 0$) is chosen to be the plane which is the mid-plane for most portions of the plate. The z-coordinate of the bottom surface of the kth layer from the bottom is denoted as z_{k-1}, and its material symmetry axis x_1 is at angle θ^k to the x-axis. The layer in which the reference plane lies or for which it is the bottom surface is denoted as the k_0th layer.

Like most other 2D plate theories, the transverse normal stress σ_z is neglected ($\sigma_z \simeq 0$) in comparison with other stress components. However, the transverse normal strain ε_z is not assumed to be zero. Using this assumption, the linear constitutive equations relating the stresses σ, τ and electric displacements D_x, D_y, D_z to

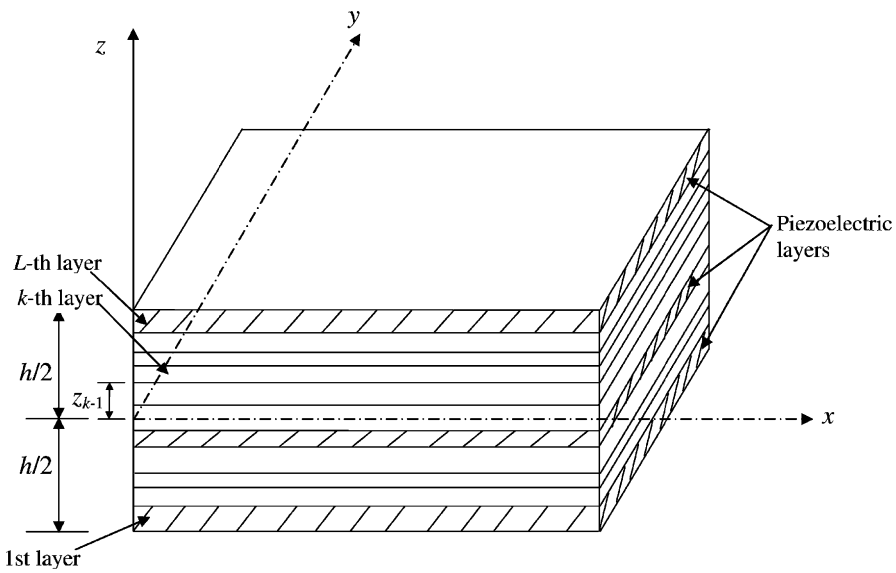

Fig. 1. Geometry of a hybrid plate segment.

the strains ε, γ and electric field components E_x, E_y, E_z are obtained as

$$\sigma = \bar{Q}\varepsilon - \bar{e}_3^{\mathrm{T}} E_z, \quad \tau = \hat{Q}\gamma - \hat{e}E, \quad D = \hat{e}^{\mathrm{T}}\gamma + \hat{\eta}E, \quad D_z = \bar{e}_3\varepsilon + \bar{\eta}_{33}E_z, \tag{1}$$

where, for general angle-ply laminas,

$$\sigma = \begin{bmatrix} \sigma_x \\ \sigma_y \\ \tau_{xy} \end{bmatrix}, \quad \tau = \begin{bmatrix} \tau_{zx} \\ \tau_{yz} \end{bmatrix}, \quad D = \begin{bmatrix} D_x \\ D_y \end{bmatrix}, \quad \varepsilon = \begin{bmatrix} \varepsilon_x \\ \varepsilon_y \\ \gamma_{xy} \end{bmatrix}, \quad \gamma = \begin{bmatrix} \gamma_{zx} \\ \gamma_{yz} \end{bmatrix}, \quad E = \begin{bmatrix} E_x \\ E_y \end{bmatrix},$$

$$\bar{Q} = \begin{bmatrix} \bar{Q}_{11} & \bar{Q}_{12} & \bar{Q}_{16} \\ \bar{Q}_{12} & \bar{Q}_{22} & \bar{Q}_{26} \\ \bar{Q}_{16} & \bar{Q}_{26} & \bar{Q}_{66} \end{bmatrix}, \quad \hat{Q} = \begin{bmatrix} \bar{Q}_{55} & \bar{Q}_{54} \\ \bar{Q}_{45} & \bar{Q}_{44} \end{bmatrix}, \quad \hat{e} = \begin{bmatrix} \bar{e}_{15} & \bar{e}_{25} \\ \bar{e}_{14} & \bar{e}_{24} \end{bmatrix}, \quad \hat{\eta} = \begin{bmatrix} \bar{\eta}_{11} & \bar{\eta}_{12} \\ \bar{\eta}_{12} & \bar{\eta}_{22} \end{bmatrix},$$

$$\bar{e}_3 = [\bar{e}_{31} \;\; \bar{e}_{32} \;\; \bar{e}_{36}]. \tag{2}$$

$\bar{Q}_{ij}, \bar{e}_{ij}$ and $\bar{\eta}_{ij}$ are the reduced elastic stiffnesses, piezoelectric stress constants and electric permittivities, which can be expressed, for a given orientation θ^k of the material axis x_1, in terms of Young's moduli Y_i, shear moduli G_{ij}, Poisson's ratios ν_{ij}, piezoelectric strain constants d_{ij} and electric permittivities η_{ij}. Let u_x, u_y and w be the inplane and transverse displacements, and ϕ be the electric potential. Denoting differentiation by a subscript comma, the strain–displacement relations and the electric field-potential relations are given by

$$\varepsilon_x = u_{x,x}, \quad \varepsilon_y = u_{y,y}, \quad \varepsilon_z = w_{,z}, \quad \gamma_{xy} = u_{x,y} + u_{y,x}, \quad \gamma_{yz} = u_{y,z} + w_{,y}, \quad \gamma_{zx} = u_{x,z} + w_{,x},$$

$$E_x = -\phi_{,x}, \quad E_y = -\phi_{,y}, \quad E_z = -\phi_{,z}. \tag{3}$$

3D coupled piezoelasticity solutions [23,29] for piezoelectric plates poled along the thickness direction have revealed that the electric potential ϕ follows a nearly quadratic distribution across the thickness. Accordingly, ϕ at time t is assumed to be piecewise quadratic between n_ϕ points at $z = z_\phi^j$ across the thickness (Fig. 2):

$$\phi(x, y, z, t) = \Psi_\phi^j(z)\phi^j(x, y, t) + \Psi_c^l(z)\phi_c^l(x, y, t), \tag{4}$$

where $\phi^j(x, y, t)$ is the electric potential at $z = z_\phi^j$ and $\phi_c^l(x, y, t)$ denotes the quadratic component of electric potential at $z = (z_\phi^l + z_\phi^{l+1})/2$. The summation convention is used with the indices j and l taking values

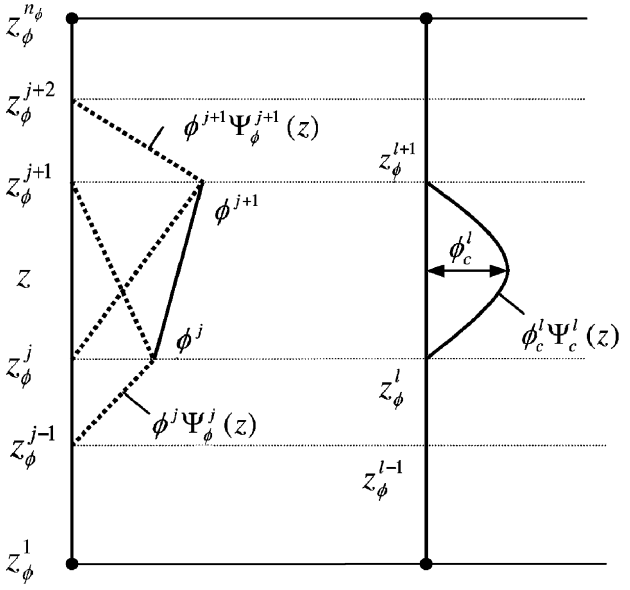

Fig. 2. Approximation of ϕ along the z-direction.

$j = 1, 2, \ldots, n_\phi$ and $l = 1, 2, \ldots, n_\phi - 1$. $\Psi^j_\phi(z)$ and $\Psi^l_c(z)$ are the piecewise linear and quadratic functions, respectively, given by

$$\Psi^j_\phi(z) = \left\{ \begin{array}{ll} 0 & \text{if } \leqslant z^{j-1}_\phi \text{ or if } z \geqslant z^{j+1}_\phi \\ (z - z^{j-1}_\phi)/(z^j_\phi - z^{j-1}_\phi) & \text{if } z^{j-1}_\phi < z < z^j_\phi \\ (z^{j+1}_\phi - z)/(z^{j+1}_\phi - z^j_\phi) & \text{if } z^j_\phi < z < z^{j+1}_\phi \end{array} \right\},$$

$$\Psi^l_c(z) = \left\{ \begin{array}{ll} 4(z^{l+1}_\phi - z)(z - z^l_\phi)/(z^{l+1}_\phi - z^l_\phi)^2 & \text{if } z^l_\phi \leqslant z \leqslant z^{l+1}_\phi \\ 0 & \text{other wise} \end{array} \right\}. \tag{5}$$

The surfaces of the piezoelectric sensor and actuator patches are always electroded with a metallic coating, which makes the surfaces equipotential. Thus, ϕ^j should be taken as independent of x, y in a finite element covering the electroded patch. With this description, ϕ in the piezoelectric layer can be modelled by a single-layer discretization, unlike the multiple sublayer discretization in case of a piecewise linear description [29].

Deflection w is approximated by integrating the constitutive equation for ε_z by including only the predominant contribution of E_z through the piezoelectric constant d_{33}. Thus, integrating $\varepsilon_z = w_{,z} \simeq -\bar{d}_{33}\phi_{,z}$ yields

$$w(x, y, z, t) = w_0(x, y, t) - \{\bar{\Psi}^j_\phi(z)\phi^j(t) + \bar{\Psi}^l_c(z)\phi^l_c(x, y, t)\}, \tag{6}$$

where $\bar{\Psi}^j_\phi(z) = \int_0^z \bar{d}_{33}\Psi^j_{\phi,z}(z)\,\mathrm{d}z$ and $\bar{\Psi}^l_c = \int_0^z \bar{d}_{33}\Psi^l_{c,z}(z)\,\mathrm{d}z$. For the kth layer, u_x, u_y are approximated as a combination of third-order variation in z across the thickness and layerwise piecewise linear variation:

$$u(x, y, z, t) = u_k(x, y, t) - zw_{0_d}(x, y, t) + z\psi_k(x, y, t) + z^2\xi(x, y, t) + z^3\eta(x, y, t), \tag{7}$$

where

$$u = \begin{bmatrix} u_x \\ u_y \end{bmatrix}, \quad w_{0_d} = \begin{bmatrix} w_{0,x} \\ w_{0,y} \end{bmatrix}, \quad u_k = \begin{bmatrix} u_{k_x} \\ u_{k_y} \end{bmatrix}, \quad \psi_k = \begin{bmatrix} \psi_{k_x} \\ \psi_{k_y} \end{bmatrix}, \quad \xi = \begin{bmatrix} \xi_x \\ \xi_y \end{bmatrix}, \quad \eta = \begin{bmatrix} \eta_x \\ \eta_y \end{bmatrix}. \tag{8}$$

u_k denotes the translation components of the kth layer and ψ_k is related to its shear rotations. ξ and η are the global quadratic and cubic terms in z. Thus, u_k and ψ_k represent the layerwise linear component of the assumed displacement field and the remaining terms in Eq. (7) represent the global third-order variation. For the mid-plane which passes through the k_0th layer, denote $u_0(x, y, t) = u_{k_0}(x, y, t) = u(x, y, 0, t)$ and $\psi_0(x, y, t) = \psi_{k_0}(x, y, t)$.

Substituting u_x, u_y, w from Eqs. (6) and (7), and ϕ from Eq. (4) into Eqs. (1) and using Eq. (2) yields the transverse shear stresses τ as

$$\tau = \hat{Q}^k[\psi_k + 2z\xi + 3z^2\eta] + [\hat{e}^k\Psi^j_\phi(z) - \hat{Q}^k\bar{\Psi}^j_\phi(z)]\phi^j_d + [\hat{e}^k\Psi^l_c(z) - \hat{Q}^k\bar{\Psi}^l_c(z)]\phi^l_{c_d}, \tag{9}$$

where $\phi^j_d = [\phi^j_{,x}\ \phi^j_{,y}]^{\mathrm{T}}$ and $\phi^l_{c_d} = [\phi^l_{c,x}\ \phi^l_{c,y}]^{\mathrm{T}}$. At interface $z = z_{i-1}$ between layers i and $i-1$, Ψ^l_c and $\bar{\Psi}^l_c$ disappear. Also, $\phi^j_{,x}, \phi^j_{,y}$ are zero in an element because of the equipotential condition of the surfaces of piezoelectric layers. Therefore, at a layer interface (as well as at the top and bottom surfaces for the same reason), all terms in Eq. (9) involving ϕ disappear. Thus, the continuity condition of τ at interface $z = z_{i-1}$ yields

$$\hat{Q}^i[\psi_i + 2z_{i-1}\xi + 3z^2_{i-1}\eta] = \hat{Q}^{i-1}[\psi_{i-1} + 2z_{i-1}\xi + 3z^2_{i-1}\eta]. \tag{10}$$

Using Eq. (10) and enforcing $(L-1)$ conditions each for the continuity of τ and u at the layer interfaces and the four shear traction-free conditions $\tau = 0$ at $z = z_0, z_L$, the $(4 + L)$ unknowns u_k, ψ_k, ξ and η for the L-layered laminate are expressed in terms of only four variables u_0 and ψ_0 to yield

$$u(x, y, z, t) = u_0(x, y, t) - zw_{0_d}(x, y, t) + R^k(z)\psi_0(x, y, t), \tag{11}$$

where $R^k(z)$ is a 2×2 matrix of the layerwise function of z of the form

$$R^k(z) = \hat{R}_1^k + z\hat{R}_2^k + z^2\hat{R}_3 + z^3\hat{R}_4. \tag{12}$$

$\hat{R}_1^k, \hat{R}_2^k, \hat{R}_3$ and $\hat{R}_4$ are 2×2 coefficient matrices which depend on the material properties and the lay-ups.

For the smeared third-order theory (TOT) [21], u can be expressed in the form of Eq. (11) with $R^k(z)$ being replaced by a diagonal matrix $R(z)$ of a global function in z for the entire thickness, defined by

$$R(z) = [z + \{-z^2(z_0+z_L)/2 + z^3/3\}/z_0 z_L]I_2, \tag{13}$$

where I_2 is a 2×2 identity matrix. Eq. (11) is expressed as

$$u = f_0(z)\bar{u}_1 \tag{14}$$

with

$$\bar{u}_1 = [u_{0_x}\ \ u_{0_y}\ \ -w_{0,x}\ \ -w_{0,y}\ \ \psi_{0_x}\ \ \psi_{0_y}]^{\mathrm{T}},$$

$$f_0(z) = [I_2\ \ I_2 z\ \ R^k(z)]. \tag{15}$$

Substitution of Eqs. (4), (6) and (11) into the field-gradient relations (3) and Eq. (2) yields

$$\varepsilon = f_1(z)\bar{\varepsilon}_1, \quad \gamma = f_2(z)\bar{\varepsilon}_2, \quad E = -f_3(z)\bar{\varepsilon}_3, \quad E_z = -f_4(z)\bar{\varepsilon}_4, \tag{16}$$

where

$$\bar{\varepsilon}_1 = [\varepsilon^0\ \ \kappa^0\ \ \psi_{0_d}]^{\mathrm{T}}, \quad f_1(z) = [I_3\ \ zI_3\ \ \bar{\Phi}^k(z)],$$

$$\bar{\varepsilon}_2 = [\psi_0\ \ -\phi_{c_d}^l]^{\mathrm{T}}, \quad f_2(z) = [R_{,z}^k(z)\ \ \bar{\Psi}_c^l(z)I_2],$$

$$\bar{\varepsilon}_3 = [\phi_{c,x}^l\ \ \phi_{c,y}^l]^{\mathrm{T}}, \quad f_3(z) = \Psi_c^l(z),$$

$$\bar{\varepsilon}_4 = [\phi_c^l\ \ \phi^j]^{\mathrm{T}}, \quad f_4(z) = [\Psi_{c,z}^l(z)\ \ \Psi_{\phi,z}^j(z)] \tag{17}$$

with

$$\varepsilon^0 = \begin{bmatrix} u_{0_{x,x}} \\ u_{0_{y,y}} \\ u_{0_{x,y}} + u_{0_{y,x}} \end{bmatrix}, \quad \kappa^0 = -\begin{bmatrix} w_{0,xx} \\ w_{0,yy} \\ 2w_{0,xy} \end{bmatrix}, \quad \psi_{0_d} = \begin{bmatrix} \psi_{0_{x,x}} \\ \psi_{0_{x,y}} \\ \psi_{0_{y,x}} \\ \psi_{0_{y,y}} \end{bmatrix}, \quad \Phi^k = \begin{bmatrix} R_{11}^k & 0 & R_{12}^k & 0 \\ 0 & R_{21}^k & 0 & R_{22}^k \\ R_{21}^k & R_{11}^k & R_{22}^k & R_{12}^k \end{bmatrix}. \tag{18}$$

3. Extended Hamilton's principle

Let p_z^1, p_z^2 be the forces per unit area applied on the bottom and top surfaces of the plate in direction z and ρ^k be the material mass density of the kth layer. The extended Hamilton's principle for the piezoelectric medium [37] can be expressed, using the notation $\langle \ldots \rangle = \sum_{k=1}^{L} \int_{z_{k-1}^+}^{z_k^-} (\ldots)\,\mathrm{d}z$ for integration across the thickness, as

$$\int_A [\langle \rho^k(\delta u^{\mathrm{T}}\ddot{u} + \ddot{w}\,\delta w) + \delta\varepsilon^{\mathrm{T}}\sigma + \delta\gamma^{\mathrm{T}}\tau - \delta E^{\mathrm{T}} D - D_z\,\delta E_z\rangle - p_z^1\,\delta w(x,y,z_0,t) - p_z^2\,\delta w(x,y,z_L,t)$$
$$+ D_z(x,y,z_0,t)\delta\phi^1 - D_z(x,y,z_L,t)\delta\phi^{n_\phi}]\,\mathrm{d}A - \int_{\Gamma_L} \langle \sigma_n\,\delta u_n + \tau_{ns}\,\delta u_s + \tau_{nz}\,\delta w + D_n\,\delta\phi\rangle\,\mathrm{d}s = 0 \tag{19}$$

$\forall \delta u_0, \delta w_0, \delta\psi_0, \delta\phi_c^l, \delta\phi^j$, where A denotes the mid-plane surface area of the plate and Γ_L is the boundary curve of the mid-plane of the plate with normal n and tangent s. It has been observed elsewhere [38] that the explicit contribution of electric potential terms in w [Eq. (6)] to inertia can be neglected to achieve computational

efficiency, without practically sacrificing any accuracy. Considering this and substituting Eqs. (4), (6), (14) and (16) into Eq. (19) yields

$$\int_A [\delta u_1^{\mathrm{T}} I\ddot{u}_1 + \delta w_0^{\mathrm{T}} \bar{I}\ddot{w}_0 + \delta\bar{\varepsilon}_1^{\mathrm{T}} F_1 + \delta\bar{\varepsilon}_2^{\mathrm{T}} F_2 + \delta\bar{\varepsilon}_3^{\mathrm{T}} F_3 + \delta\bar{\varepsilon}_4^{\mathrm{T}} F_4 - P_3\,\delta w_0 - P_\phi^j\,\delta\phi^j]\,\mathrm{d}A$$
$$- \int_{\Gamma_L} [N_n\,\delta u_{0_n} + N_{ns}\,\delta u_{0_s} - M_n\,\delta w_{0,n} + (V_n + M_{ns,s})\delta w_0 + P_n\,\delta\psi_{0_n} + P_{ns}\,\delta\psi_{0_s}$$
$$+ (H_n^j - V_{\phi_n}^j)\,\delta\phi^j + (H_{c_n}^l - V_{c_n}^l)\,\delta\phi_c^l]\,\mathrm{d}s - \sum_i \Delta M_{ns}(s_i)\,\delta w_0(s_i) = 0, \tag{20}$$

where the lateral surface has corners at $s = s_i$. In this equation, I and $\bar{I}$ are the inertia matrices defined by

$$I = \langle \rho^k f_0^{\mathrm{T}}(z) f_0(z)\rangle = \begin{bmatrix} I_{11} & 0 & I_{13} & 0 & I_{15} & I_{16} \\ 0 & I_{22} & 0 & I_{24} & I_{25} & I_{26} \\ I_{31} & 0 & I_{33} & 0 & I_{35} & I_{36} \\ 0 & I_{42} & 0 & I_{44} & I_{45} & I_{46} \\ I_{51} & I_{52} & I_{53} & I_{54} & I_{55} & I_{56} \\ I_{61} & I_{62} & I_{63} & I_{64} & I_{65} & I_{66} \end{bmatrix}, \quad \bar{I} = \langle \rho^k \rangle = I_{11} \tag{21}$$

with the following explicit expressions for the submatrices:

$$\left[\begin{bmatrix} I_{11} & 0 \\ 0 & I_{22} \end{bmatrix}, \begin{bmatrix} I_{13} & 0 \\ 0 & I_{24} \end{bmatrix}, \begin{bmatrix} I_{15} & I_{16} \\ I_{25} & I_{26} \end{bmatrix}\right] = \langle \rho^k [I_2,\ zI_2,\ R^k(z)]\rangle,$$

$$\left[\begin{bmatrix} I_{33} & 0 \\ 0 & I_{44} \end{bmatrix}, \begin{bmatrix} I_{35} & I_{36} \\ I_{45} & I_{46} \end{bmatrix}, \begin{bmatrix} I_{55} & I_{56} \\ I_{65} & I_{66} \end{bmatrix}\right] = \langle \rho^k [z^2 I_2,\ zR^k(z), \{R^k(z)\}^{\mathrm{T}} R^k(z)]\rangle. \tag{22}$$

The stress resultants F_1 of σ and F_2, V, V_ϕ^j, V_c^l of τ, and the electric displacement resultants F_3, H^j of D and F_4 of D_z are defined by

$$F_1 = [N^{\mathrm{T}}\ \ M^{\mathrm{T}}\ \ P^{\mathrm{T}}]^{\mathrm{T}} = [\langle f_1^{\mathrm{T}}\sigma\rangle], \quad F_2 = [Q^{\mathrm{T}}\ \ \bar{Q}^{l^{\mathrm{T}}}]^{\mathrm{T}} = [\langle f_2^T \tau\rangle],$$

$$F_3 = [H_{c_x}^l\ \ H_{c_y}^l]^{\mathrm{T}} = \langle f_3(z) D\rangle, \quad F_4 = [G_c^l\ \ G^j]^{\mathrm{T}} = [\langle f_4^T D_z\rangle], \quad V = [V_x\ \ V_y]^{\mathrm{T}} = \langle\tau\rangle,$$

$$V_\phi^j = [V_{\phi_x}^j\ \ V_{\phi_y}^j]^{\mathrm{T}} = \langle \bar{\Psi}_\phi^j \tau\rangle, \quad V_c^l = [V_{c_x}^l\ \ V_{c_y}^l]^{\mathrm{T}} = \langle \bar{\Psi}_c^l \tau\rangle, \quad H^j = [H_x^j\ \ H_y^j]^{\mathrm{T}} = \langle \Psi_\phi^j D\rangle,$$

$$N = [N_x\ \ N_y\ \ N_{xy}]^{\mathrm{T}}, \quad M = [M_x\ \ M_y\ \ M_{xy}]^{\mathrm{T}}, \quad P = [P_x\ \ P_{yx}\ \ P_{xy}\ \ P_y],$$

$$Q = [Q_x\ \ Q_y]^{\mathrm{T}}, \quad \bar{Q}^l = [\bar{Q}_x^l\ \ \bar{Q}_y^l]^{\mathrm{T}}. \tag{23}$$

N, M and P denote the inplane force, moment and higher order moment resultants, respectively. V and Q denote the transverse shear and higher order transverse shear resultants, respectively, and V_ϕ^j, V_c^l and $\bar{Q}^l$ are the electromechanical transverse shear resultants. It can be shown that elements of R^k, N, M and P transform as second-order tensors and elements of $V, V_\phi^j, V_c^l, Q, \bar{Q}^l, H^j, H_c^l$ transform as vectors for the coplanar axes x, y and n, s. The mechanical load P_3 and the electromechanical loads P_ϕ^j in Eq. (20) are defined by

$$P_3 = p_z^1 + p_z^2, \quad P_\phi^j = -p_z^1 \bar{\Psi}_\phi^j(z_0) - p_z^2 \bar{\Psi}_\phi^j(z_L) + D_z(x, y, z_L, t)\delta_{jn_\phi} - D_z(x, y, z_0, t)\delta_{j1}, \tag{24}$$

where δ_{ij} is Kronecker's delta. Substitution of the constitutive equations (1) into Eq. (23) yields the following generalized piezoelectric plate constitutive equations:

$$F_1 = A\bar{\varepsilon}_1 + \beta\bar{\varepsilon}_4, \quad F_2 = \bar{A}\bar{\varepsilon}_2 + \bar{\beta}\bar{\varepsilon}_3, \quad F_3 = \bar{\beta}^{\mathrm{T}}\bar{\varepsilon}_2 + \bar{E}\bar{\varepsilon}_3, \quad F_4 = \beta^{\mathrm{T}}\bar{\varepsilon}_1 + \bar{F}\bar{\varepsilon}_4, \tag{25}$$

where

$$A = \langle f_1^{\mathrm{T}}(z)\bar{Q}f_1(z)\rangle, \quad \beta = \langle f_1^{\mathrm{T}}(z)\bar{e}_3^{\mathrm{T}}f_4(z)\rangle, \quad \bar{F} = -\langle \bar{\eta}_{33}f_4^{\mathrm{T}}(z)f_4(z)\rangle,$$

$$\bar{A} = \langle f_2^{\mathrm{T}}(z)\hat{Q}f_2(z)\rangle, \quad \bar{\beta} = \langle f_2^{\mathrm{T}}(z)\hat{e}\Psi_c^{l'}(z)\rangle, \quad \bar{E} = -\langle \hat{\eta}\Psi_c^{l}(z)\Psi_c^{l'}(z)\rangle. \tag{26}$$

Using the generalized constitutive equations (25), the area integral in Eq. (20) reduces to

$$\int_A [\delta u_1^{\mathrm{T}} I\ddot{\bar{u}}_1 + \delta w_0^{\mathrm{T}}\bar{I}\ddot{\bar{w}}_0]\,\mathrm{d}A + \int_A [\delta\bar{\varepsilon}_1^{\mathrm{T}}A\bar{\varepsilon}_1 + \delta\bar{\varepsilon}_1^{\mathrm{T}}\beta\bar{\varepsilon}_4 + \delta\bar{\varepsilon}_2^{\mathrm{T}}\bar{A}\bar{\varepsilon}_2 + \delta\bar{\varepsilon}_2^{\mathrm{T}}\bar{\beta}\bar{\varepsilon}_3 + \delta\bar{\varepsilon}_3^{\mathrm{T}}\bar{\beta}^{\mathrm{T}}\bar{\varepsilon}_2 + \delta\bar{\varepsilon}_3^{\mathrm{T}}\bar{E}\bar{\varepsilon}_3 + \delta\bar{\varepsilon}_4^{\mathrm{T}}\beta^{\mathrm{T}}\bar{\varepsilon}_1 + \delta\bar{\varepsilon}_4^{\mathrm{T}}\bar{F}\bar{\varepsilon}_4 - P_3\,\delta w_0 - P_\phi^j\,\delta\phi^j]\,\mathrm{d}A. \tag{27}$$

The variationally consistent boundary conditions on Γ_L are obtained from the terms in the line integral in Eq. (20) as the prescribed values of one of the factors of each of the following products:

$$u_{0_n}N_n, \quad u_{0_s}N_{ns}, \quad w_0(V_n + M_{ns,s}), \quad w_{0,n}M_n, \quad \psi_{0_n}P_n, \quad \psi_{0_s}P_{ns}, \quad \phi^j[H_n^j - V_{\phi_n}^j], \quad \phi_c^l[H_{c_n}^l - V_{c_n}^l]$$
$$\text{and at corners } s_i\text{: } w_0(s_i)\Delta M_{ns}(s_i). \tag{28}$$

The mechanical boundary conditions for various edge conditions are

$$\text{simply supported: } N_n = 0, \quad u_{0_s} = 0, \quad w_0 = 0, \quad M_n = 0, \quad P_n = 0, \quad \psi_{0_s} = 0,$$

$$\text{clamped: } u_{0_n} = 0, \quad u_{0_s} = 0, \quad w_0 = 0, \quad w_{0,n}(=\theta_n) = 0, \quad \psi_{0_n} = 0, \quad \psi_{0_s} = 0,$$

$$\text{free: } N_n = 0, \quad N_{ns} = 0, \quad V_n + M_{ns,s} = 0, \quad M_n = 0, \quad P_n = 0, \quad P_{ns} = 0. \tag{29}$$

4. Finite element formulation

A four-node quadrilateral element is developed based on the coupled improved zigzag theory presented above. While the electric variables ϕ_c^l are a function of inplane coordinates (x, y), ϕ^j is constant over the element. In a novel hybrid approach, ϕ_c^l is treated as nodal dof and ϕ^j is treated as elemental dof. However, if a number of elements fall in the same electroded surface, it would be necessary to impose the constraint of equality on the electric dof ϕ^j of the elements on the same electroded surface. Instead, the set of ϕ^j of the equipotential surfaces of piezoelectric patches in a plate section is associated with a separate *electric node* p (Fig. 3), which can be connected to several elements. The electric node does not have any physical coordinates

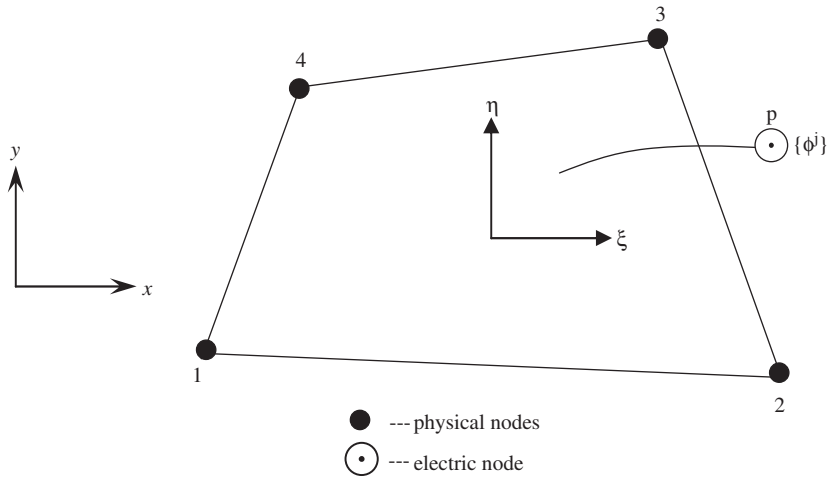

Fig. 3. The quadrilateral element with an electric node.

unlike the physical nodes, and has n_ϕ degrees of freedom. This concept not only eliminates the need for imposing equality constraints on the electric dof for an equipotential condition but also results in a significant reduction in the number electric dof.

As the highest derivatives of $u_{0_x}, u_{0_y}, \psi_{0_x}, \psi_{0_y}, \phi_c^l$ appearing in variational equation (20) are of first order, the convergence criteria require their interpolation function to be C^0 continuous at the element boundary. Accordingly, these variables are interpolated using bilinear Lagrange interpolation functions, N_i $(i = 1, 2, 3, 4)$, as

$$u_{0_x} = Nu_{0_x}^e, \quad u_{0_y} = Nu_{0_y}^e, \quad \psi_{0_x} = N\psi_{0_x}^e, \quad \psi_{0_y} = N\psi_{0_y}^e, \quad \phi_c^l = N\phi_c^{l^e}, \tag{30}$$

where

$$u_{0_x}^e = [u_{0_x}^1 \;\; u_{0_x}^2 \;\; u_{0_x}^3 \;\; u_{0_x}^4]^T, \quad u_{0_y}^e = [u_{0_y}^1 \;\; u_{0_y}^2 \;\; u_{0_y}^3 \;\; u_{0_y}^4]^T,$$

$$\psi_{0_x}^e = [\psi_{0_x}^1 \;\; \psi_{0_x}^2 \;\; \psi_{0_x}^3 \;\; \psi_{0_x}^4]^T, \quad \psi_{0_y}^e = [\psi_{0_y}^1 \;\; \psi_{0_y}^2 \;\; \psi_{0_y}^3 \;\; \psi_{0_y}^4]^T,$$

$$\phi_c^{l^e} = [\phi_c^{l^1} \;\; \phi_c^{l^2} \;\; \phi_c^{l^3} \;\; \phi_c^{l^4}]^T, \quad N = [N_1 \;\; N_2 \;\; N_3 \;\; N_4]. \tag{31}$$

The presence of the second derivative of w_0 in Eq. (20) indicates that its interpolation function should have C^1 continuity at the element boundary, which is difficult to achieve for a quadrilateral element [39]. The need for C^1 continuity is circumvented herein by using the improved discrete Kirchhoff constraint approach, which was proposed in Ref. [40] for the bending of isotropic thin Kirchhoff plates and successfully employed for elastic anisotropic laminated plates by the authors [36]. In this approach, $w_{0,x}$, $w_{0,y}$ are replaced by rotation variables θ_{0_x}, θ_{0_y}, which then require only C^0 continuity. w_0 and $\theta_{0_x}, \theta_{0_y}$ are interpolated independently, but the two are subsequently related by imposing the constraints $\theta_{0i} = w_{0,i}$ at discrete points on the element boundary as well as in the interior. The implementation enforces complete compatibility of the deflection field along the element sides [39]. However, due to discrete imposition of constraints, its convergence characteristics are not clear *a priori*, as for the non-conforming elements. w_0 is interpolated assuming a bicubic function in terms of parametric co-ordinates ξ and η [39] as

$$w_0 = [\tilde{N}_1 \;\; \tilde{N}_2 \;\; \tilde{N}_3 \;\; \tilde{N}_4 \;\; \tilde{N}_5 \;\; \tilde{N}_6 \;\; \tilde{N}_7 \;\; \tilde{N}_8 \;\; \tilde{N}_9 \;\; \tilde{N}_{10} \;\; \tilde{N}_{11} \;\; \tilde{N}_{12}]w_0^e = \tilde{N}w_0^e, \tag{32}$$

where

$$w_0^e = [w_0^1 \;\; w_{0,x}^1 \;\; w_{0,y}^1 \;\; w_0^2 \;\; w_{0,x}^2 \;\; w_{0,y}^2 \;\; w_0^3 \;\; w_{0,x}^3 \;\; w_{0,y}^3 \;\; w_0^4 \;\; w_{0,x}^4 \;\; w_{0,y}^4]^T. \tag{33}$$

The expressions for $\tilde{N}_i$ can be found in Ref. [36]. The rotations $\theta_{0_x}, \theta_{0_y}$ are originally interpolated in terms of their values $\theta_{0_x}^i$, $\theta_{0_y}^i$ at the nine nodes $(i = 1, 2, \ldots, 9)$ of a Lagrange element, namely, nodes 1–4 at the corners, nodes 5–8 at the mid sides and node 9 at the center:

$$\theta_{0_x} = \bar{N}\theta_{0_x}^e, \quad \theta_{0_y} = \bar{N}\theta_{0_y}^e, \tag{34}$$

where

$$\theta_{0i}^e = [\theta_{0i}^1 \quad \theta_{0i}^2 \quad \ldots \quad \theta_{0i}^9]^T, \quad i = x, y; \quad \bar{N} = [\bar{N}_1 \quad \bar{N}_2 \quad \ldots \quad \bar{N}_9]. \tag{35}$$

$\bar{N}_i$ are the smoothed interpolation functions obtained from standard Lagrange interpolation functions through a least-square fit [40]. The 18 nodal rotation variables $\theta_{0_x}^i$, $\theta_{0_y}^i$ for nine nodes are related to deflection vector w_0^e of the four corner nodes by imposing 18 conditions on the former. Let θ_s and θ_n be the direction derivatives of w along the tangent s to an edge and along its normal n, respectively. The constraints $\theta_{0_x}^i = w_{0,x}^i$

and $\theta^i_{0_y} = w^i_{0,y}$ are imposed at the four corner nodes $i = 1$–4, and at the interior node 9, yielding ten conditions. The remaining eight conditions are as follows:

1. Impose at mid-side nodes i of side jl joining corner nodes j and l ($i = 5$–8) the constraints $\theta^i_s = w^i_{0,s}$ where $w^i_{0,s}$ is obtained by considering the cubic variation of w along the side of length a_{jl} as

$$\begin{aligned} w^i_{,s} &= -\frac{3}{2a_{jl}}(w^j_0 - w^l_0) - \frac{1}{4}(w^j_{0,s} + w^l_{0,s}) \\ &= -\frac{3}{2a_{jl}}(w^j_0 - w^l_0) - \frac{1}{4}[(w_{0,x}s_x + w_{0,y}s_y)^j + (w_{0,x}s_x + w_{0,y}s_y)^l]. \end{aligned} \tag{36}$$

2. Approximate the variation of θ_n to be linear along each side, i.e.,

$$\theta^i_n = \tfrac{1}{2}(\theta^j_n + \theta^l_n) \Rightarrow (w_{0,x}n_x + w_{0,y}n_y)^i = \tfrac{1}{2}\{(w_{0,x}n_x + w_{0,y}n_y)^j + (w_{0,x}n_x + w_{0,y}n_y)^l\}. \tag{37}$$

Thus, θ_{0_x}, θ_{0_y} are finally expressed in terms of w^e_0 as

$$\theta_{0_x} = Gw^e_0, \quad \theta_{0_y} = Hw^e_0, \tag{38}$$

where

$$G = [G_1 \quad G_2 \quad \ldots \quad G_{12}], \quad H = [H_1 \quad H_2 \quad \ldots \quad H_{12}].$$

The expressions of the interpolation functions G_i and H_i are available in Ref. [36]. For the purpose of comparison, the DKQ interpolation functions of Batoz and Tahar [41] are also employed for $\theta_{0_x}, \theta_{0_y}$. In this case, $\theta_{0_x}, \theta_{0_y}$ are originally interpolated using an eight-node serendipity element instead of the nine-node Lagrange element, and the constraints $\theta_{0_x} = w_{0,x}$ and $\theta_{0_y} = w_{0,y}$ are not imposed in any interior point of the element.

The generalized displacement vector U^e of the element is defined in terms of the nodal variables U^e_i of the physical nodes, $i = 1, 2, 3, 4$, and ϕ^j of the electric node as

$$U^e_i = [u^i_{0_x} \quad u^i_{0_y} \quad w^i_0 \quad w^i_{0,x} \quad w^i_{0,y} \quad \psi^i_{0_x} \quad \psi^i_{0_y} \quad \phi^{l^i}_c]^{\mathrm{T}}, \qquad l = 1, 2, \ldots, n_\phi - 1,$$

$$U^{e\mathrm{T}} = [U^{e\mathrm{T}}_1 \quad U^{e\mathrm{T}}_2 \quad U^{e\mathrm{T}}_3 \quad U^{e\mathrm{T}}_4 \quad \phi^j], \quad j = 1, 2, \ldots, n_\phi. \tag{39}$$

Using Eqs. (15), (30), (32) and (38), $\bar{u}_1$, w_0 and ϕ^j are expressed in terms of U^e as

$$\bar{u}_1 = N_u U^e, \qquad w_0 = N_w U^e, \qquad \phi^j = N_\phi U^e \tag{40}$$

where

$$\begin{aligned} N_u &= [N^1_u \quad N^2_u \quad N^3_u \quad N^4_u \quad 0]U^e, \\ N_w &= [N^1_w \quad N^2_w \quad N^3_w \quad N^4_w \quad 0]U^e, \\ N_\phi &= [0 \quad 0 \quad 0 \quad 0 \quad 1]U^e, \\ N^i_u &= \begin{bmatrix} N_i & 0 & 0 & 0 & 0 & 0 & 0 & 0 \\ 0 & N_i & 0 & 0 & 0 & 0 & 0 & 0 \\ 0 & 0 & -G_{3i-2} & -G_{3i-1} & -G_{3i} & 0 & 0 & 0 \\ 0 & 0 & -H_{3i-2} & -H_{3i-1} & -H_{3i} & 0 & 0 & 0 \\ 0 & 0 & 0 & 0 & 0 & N_i & 0 & 0 \\ 0 & 0 & 0 & 0 & 0 & 0 & N_i & 0 \end{bmatrix}, \\ N^i_w &= [0 \quad 0 \quad \tilde{N}_{3i-2} \quad \tilde{N}_{3i-1} \quad \tilde{N}_{3i} \quad 0 \quad 0 \quad 0]. \end{aligned} \tag{41}$$

The generalized strains $\bar{\varepsilon}_i$ in Eq. (17) are expressed in terms of U^e as

$$\bar{\varepsilon}_i = B_i U^e, \qquad i = 1, 2, 3, 4, \tag{42}$$

where B_i are the generalized strain–displacement matrices given by

$$B_i = [B_i^1 \quad B_i^2 \quad B_i^3 \quad B_i^4 \quad 0] \quad \text{for } i = 1,2,3, \quad B_4 = [B_4^1 \quad B_4^2 \quad B_4^3 \quad B_4^4 \quad B_4^\phi],$$

$$B_1^i = \begin{bmatrix} \frac{\partial N_i}{\partial x} & 0 & 0 & 0 & 0 & 0 & 0 & 0 \\ 0 & \frac{\partial N_i}{\partial y} & 0 & 0 & 0 & 0 & 0 & 0 \\ \frac{\partial N_i}{\partial y} & \frac{\partial N_i}{\partial x} & 0 & 0 & 0 & 0 & 0 & 0 \\ 0 & 0 & -\frac{\partial G_{3i-2}}{\partial x} & -\frac{\partial G_{3i-1}}{\partial x} & -\frac{\partial G_{3i}}{\partial x} & 0 & 0 & 0 \\ 0 & 0 & -\frac{\partial H_{3i-2}}{\partial y} & -\frac{\partial H_{3i-1}}{\partial y} & -\frac{\partial H_{3i}}{\partial y} & 0 & 0 & 0 \\ 0 & 0 & -\frac{\partial G_{3i-2}}{\partial y} - \frac{\partial H_{3i-2}}{\partial x} & -\frac{\partial G_{3i-1}}{\partial y} - \frac{\partial H_{3i-1}}{\partial x} & -\frac{\partial G_{3i}}{\partial y} - \frac{\partial H_{3i}}{\partial x} & 0 & 0 & 0 \\ 0 & 0 & 0 & 0 & 0 & \frac{\partial N_i}{\partial x} & 0 & 0 \\ 0 & 0 & 0 & 0 & 0 & \frac{\partial N_i}{\partial y} & 0 & 0 \\ 0 & 0 & 0 & 0 & 0 & 0 & \frac{\partial N_i}{\partial x} & 0 \\ 0 & 0 & 0 & 0 & 0 & 0 & \frac{\partial N_i}{\partial y} & 0 \end{bmatrix},$$

$$B_2^i = \begin{bmatrix} 0 & 0 & 0 & 0 & 0 & N_i & 0 & 0 \\ 0 & 0 & 0 & 0 & 0 & 0 & N_i & 0 \\ 0 & 0 & 0 & 0 & 0 & 0 & 0 & -\frac{\partial N_i}{\partial x} \\ 0 & 0 & 0 & 0 & 0 & 0 & 0 & -\frac{\partial N_i}{\partial y} \end{bmatrix}, \quad B_3^i = \begin{bmatrix} 0 & 0 & 0 & 0 & 0 & 0 & 0 & \frac{\partial N_i}{\partial x} \\ 0 & 0 & 0 & 0 & 0 & 0 & 0 & \frac{\partial N_i}{\partial y} \end{bmatrix},$$

$$B_4^i = \begin{bmatrix} 0 & 0 & 0 & 0 & 0 & 0 & 0 & N_i \\ 0 & 0 & 0 & 0 & 0 & 0 & 0 & 0 \end{bmatrix}, \quad B_4^\phi = \begin{bmatrix} 0 \\ 1 \end{bmatrix}. \tag{43}$$

Substituting Eqs. (40) and (42) into Eq. (27), the contribution T^e of one element to the area integral can be obtained as

$$\begin{aligned} T^e &= \delta U^{e\mathrm{T}} \int_{A^e} [N^{u\mathrm{T}} I N^u + N^{w\mathrm{T}} \bar{I} N^w] \,\mathrm{d}x\,\mathrm{d}y\, \ddot{U}^e + \delta U^{e\mathrm{T}} \int_{A^e} [B_1^{\mathrm{T}} A B_1 + B_1^{\mathrm{T}} \beta B_4 + B_2^{\mathrm{T}} \bar{A} B_2 + B_2^{\mathrm{T}} \bar{\beta} B_3 \\ &\quad + B_3^{\mathrm{T}} \bar{\beta} B_2 + B_3^{\mathrm{T}} \bar{E} B_3 + B_4^{\mathrm{T}} \beta^{\mathrm{T}} B_1 + B_4^{\mathrm{T}} \bar{F} B_4] \,\mathrm{d}x\,\mathrm{d}y\, U^e - \delta U^{e\mathrm{T}} \int_{A^e} (N_w^{\mathrm{T}} p_z + N_\phi^{\mathrm{T}} P_\phi^j) \,\mathrm{d}x\,\mathrm{d}y \\ &= \delta U^{e\mathrm{T}} [\bar{M}^e \ddot{U}^e + \bar{K}^e U^e - \bar{P}^e], \end{aligned}$$

where $\bar{M}^e$, $\bar{K}^e$ and $\bar{P}^e$ are the element mass matrix, the element stiffness matrix and the consistent load vector. The elements with one or more sides on the boundary will contribute to the line integral part of Eq. (20). For the boundary conditions given in Eq. (29), this line integral is zero. However, there will be a contribution to the load vector for other boundary conditions where non-zero stress resultants are prescribed. For example, for an unconstrained edge with inplane edge forces, there will be contribution to the load vector for the dof $u^e_{0_x}$, $u^e_{0_y}$ for the nodes on that edge. Loads applied at nodes are added to $\bar{P}$ at locations corresponding to their global degree of freedom numbers. Summing up the contributions for all elements in Eq. (20), since the virtual

generalized displacements are arbitrary, Eq. (20) yields

$$\bar{M}\ddot{U} + \bar{K}U = \bar{P}, \tag{44}$$

where $\bar{M}$, $\bar{K}$ and $\bar{P}$ are the assembled counterparts of matrices $\bar{M}^e$, $\bar{K}^e$ and $\bar{P}^e$. The physical nodes and the electric node of each element are stored in an element connectivity matrix, and the global dof numbers of element dof of physical nodes and electric nodes are stored in separate index matrices. Assembly of the element stiffness, mass and load matrices then follows the standard procedure [42]. A 3×3 Gauss integration scheme is used for the numerical integration to obtain $\bar{M}^e$, $\bar{K}^e$ and $\bar{P}^e$ in view of a bi-cubic variation of w_0.

At the surfaces with prescribed voltage (close circuit condition), electric potentials have known prescribed values. At the surfaces with prescribed charge (open circuit condition), the electric loads are known (zero electric charge, i.e., $\int_{A_e} D_z \,\mathrm{d}x\,\mathrm{d}y = 0$, A_e being the area of the electrode), but the electric potentials are unknown. The system vector U is partitioned into vectors of mechanical displacements $\bar{U}$, unknown voltages Φ_s and known input actuation voltages Φ_a. Thus, Eq. (44) can be partitioned and arranged as

$$\begin{bmatrix} M^{uu} & 0 & 0 \\ 0 & 0 & 0 \\ 0 & 0 & 0 \end{bmatrix} \begin{Bmatrix} \ddot{\bar{U}} \\ \ddot{\Phi}_s \\ \ddot{\Phi}_a \end{Bmatrix} + \begin{bmatrix} K^{uu} & K^{us} & K^{ua} \\ K^{su} & K^{ss} & K^{sa} \\ K^{au} & K^{as} & K^{aa} \end{bmatrix} \begin{Bmatrix} \bar{U} \\ \Phi_s \\ \Phi_a \end{Bmatrix} = \begin{Bmatrix} \bar{P} \\ Q_s \\ Q_a \end{Bmatrix}. \tag{45}$$

Eq. (45) yields the output potentials as

$$\Phi_s = -(K^{ss})^{-1}[K^{su}\bar{U} + K^{sa}\Phi_a - Q_s]. \tag{46}$$

Substituting Eq. (46) into Eq. (45) and introducing Rayleigh damping with damping matrix $C^{uu} = \alpha_1 M^{uu} + \alpha_2 K^{uu}$ yields

$$M^{uu}\ddot{\bar{U}} + C^{uu}\dot{\bar{U}} + [K^{uu} - K^{us}(K^{ss})^{-1}K^{su}]\bar{U} = \bar{P} - K^{us}(K^{ss})^{-1}Q_s - [K^{ua} - K^{us}(K^{ss})^{-1}K^{sa}]\Phi_a. \tag{47}$$

For undamped free vibration, the damping matrix C^{uu} and the right-hand side vector of the above equation are set to zero. The resulting generalized eigenvalue problem is solved using the subspace iteration method [43] to obtain the undamped circular natural frequencies ω_n and the mode shapes. For a transient response, Eq. (47) can be solved using the Newmark direct time integration scheme [43]. The advantage of first partitioning the electric potential vector Φ into Φ_s and Φ_a, and then carrying out the condensation as per Eqs. (46) and (47) is that it can model the response of the structure under any electric boundary conditions, namely, in the active mode (close circuit), the sensory mode (open circuit) and the combined 'active-sensory' mode (some electrodes in an open circuit and some in a close circuit). In contrast, if the entire electric potential vector Φ is condensed out as in Ref. [12], the resulting problem would give only the open-circuit response. Vasques and Rodrigues [8], on the other hand, adopted different static condensations for electroded open circuit, non-electroded open circuit and close circuit conditions, without the possibility of a combined mode.

5. Numerical results

5.1. Validation and comparison with other solutions

For validation of the present formulation of the discrete Kirchhoff improved zigzag theory-based (DKIZIGT) element for free vibration analysis and the computer program developed, the following two problems are considered for which results have been presented by other researchers using different theories and finite elements. In addition, the relative accuracy of the present element is also assessed in direct comparison with the exact 3D piezoelasticity solution [23,24] or the 3D FE solution obtained using the commercial software ABAQUS.

5.1.1. Piezoelectric bimorph plate

A rectangular piezoelectric bimorph made of two identical layers of PZT-4 piezoceramics with the poling direction along z-axis, which was analyzed by Wang [5], is considered here. The length a and width b of the plate are 25 and 12.5 mm, respectively. The plate is simply supported at opposite edges at $x = 0, a$ with

Table 1
Natural frequencies f_n(Hz) of a bimorph plate

Entity	Mode	Close circuit			Open circuit		
		3D FE (ABAQUS)	Present IZIGT FE	FSDT FE (Wang [5])	3D FE (ABAQUS)	Present IZIGT FE	FSDT FE (Wang [5])
f_1	Flexure	5938.5	5937.6	6258	6105	6114.5	6433
f_2	Flexure	14,545	15,498	13,833	14,619	15,564	13,909
f_3	Flexure	22,871	22,801	23,814	23,459	23,523	24,473
f_4	Inplane shear	23,785	27,570	26,612	24,139	28,072	26,967
f_5	Extension	28,575	32,893	–	29,459	34,279	–
f_6	Flexure	33,805	35,078	33,057	34,094	35,462	33,452
f_7	Flexure	48,258	47,875	49,664	49,187	49,294	50,880

$w_0 = 0, u_{0_y} = 0$ at $x = 0, a$ and $u_{0_x} = 0$ at $x = 0$. The other two edges are free. The material properties of PZT-4 are taken as given in Ref. [5]:

$$[C_{11}, C_{22}, C_{33}, C_{12}, C_{23}, C_{31}, C_{44}, C_{55}, C_{66}] = [139, 139, 115, 77.8, 74.3, 74.3, 25.6, 25.6, 30.6]\,\text{GPa},$$

$$[(e_{31}, e_{32}, e_{33}, e_{15}, e_{24}), (\eta_{11}, \eta_{22}, \eta_{33})] = [(-5.2, -5.2, 15.1, 12.7, 12.7)\,\text{C/m}^2, (13.06, 13.06, 11.51)\,\text{nF/m}]$$

and $\rho = 7600\,\text{Kg/m}^3$, where C_{ij} and e_{ij} are the stiffness coefficients and piezoelectric stress constants. The interfaces between the two PZT layers are grounded. The natural frequencies $f_n (= \omega_n/2\pi)$ are obtained for the plate for span-to-thickness ratio, $S = a/h = 10$, for both close circuit ($\phi^1 = \phi^{n_\phi} = 0$) and open circuit conditions on the top and bottom surfaces. The natural frequencies for the first seven modes predicted by the present DKIZIGT element with a mesh size of 16×16 are compared in Table 1with the FSDT FE results of Wang [5]. Wang's results are obtained using 200 eight-node elements and 10 sublayer discretization of each piezoelectric layer for ϕ. The present FE results are obtained using IDKQ interpolation for the deflection. To assess the relative accuracy of these results, a coupled 3D FE analysis is performed using a 20-node piezoelectric solid element (C3D20RE) in ABAQUS with a mesh size of $40 \times 20 \times 8$ (6400 elements), yielding converged results. The corresponding results are also listed in Table 1. It is observed that the present results are in good agreement with those of Wang [5] for both close and open circuit frequencies. However, in comparison with the 3D FE solution, the present IZIGT FE yields far more accurate results for f_n than the FSDT FE [5] for the flexural modes 1, 3 and 7, which correspond to bending along the x-direction only. The maximum percent error in the present IZIGT FE results for frequencies of these modes is only 0.8% and 0.3% for the close and open circuit conditions, respectively, whereas the maximum error in the FSDT FE for the above modes is 5.4% for both electric boundary conditions. For the bi-directional bending modes 2 and 6, the error in the present IZIGT results is marginally higher than that for the FSDT. However, it may be due to a difference in the boundary conditions regarding $u_{0_y} = 0$ considered here and in Ref. [5], wherein the same has not been specified. Wang's FSDT FE missed the fifth mode which is an extension mode. It may be noted that the open circuit frequencies are higher than the close circuit ones for all modes. This can be understood from Eq. (47), by observing that the effective stiffness matrix becomes modified by the electromechanical stiffness corresponding to the open circuit potentials Φ_s.

It is pertinent to note here that the number of electric dof in the present model for this problem is $2 \times 17 \times 17 + 3 = 581$. For a similar mesh, the FE model of Wang [5] with 10 sublayers in each layer, this number would be $21 \times 16 \times 16 = 5376$. The number of electric potential dof associated with the layer surfaces is only 3 in the present modelling using an electric node for the close circuit boundary condition, whereas for the traditional concept of nodal/elemental electric variables, the same would be 867/768.

5.1.2. Hybrid composite plate of Heyliger and Saravanos [23]

The simply supported square hybrid plate analyzed by Heyliger and Saravanos [23], which consists of a substrate of a three-layer cross-ply graphite-epoxy composite ($0^\circ/90^\circ/0^\circ$) of material 1 with two layers of PZT-4 bonded to its top and bottom surfaces, is considered next. The thickness of each layer of the composite

Table 2
Material properties

Property	Unit	Mat. 1	Mat. 2	Mat. 3	Mat. 4	Mat. 5	Mat. 6	PZT-4	PZT-5A
		Ref. [23]	Ref. [30]					Ref. [23]	Ref. [29]
Y_1	GPa	132.38	6.9	224.25	172.5	131.1	0.0002208	81.3	61.0
Y_2	GPa	10.756	6.9	6.9	6.9	6.9	0.0002001	81.3	61.0
Y_3	GPa	10.756	6.9	6.9	6.9	6.9	2.760	64.5	53.2
G_{12}	GPa	5.6537	1.38	56.58	3.45	3.588	0.01656	30.6	22.6
G_{23}	GPa	3.606	1.38	1.38	1.38	2.3322	0.4554	25.6	21.1
G_{31}	GPa	5.6537	1.38	56.58	3.45	3.588	0.5451	25.6	21.1
ν_{12}		0.24	0.25	0.25	0.25	0.32	0.99	0.329	0.35
ν_{13}		0.24	0.25	0.25	0.25	0.32	3×10^{-5}	0.432	0.38
ν_{23}		0.49	0.25	0.25	0.25	0.49	3×10^{-5}	0.432	0.38
ρ	kg/m^3	1	1578	1578	1578	1000	70	1	7600
d_{31}	pm/V							−123.04748	−171
d_{32}	pm/V							−123.04748	−171
d_{33}	pm/V							289.0604	374
d_{15}	pm/V							496.875	584
d_{24}	pm/V							496.875	584
η_{11}	nF/m	0.030975						13.0537	15.3
η_{22}	nF/m	0.02655						13.0537	15.3
η_{33}	nF/m	0.02655						11.505	15.0

sublaminate is $0.267h$ and that of each PZT layer is $0.1h$. The properties of material 1, PZT-4 and other materials considered in this study are listed in Table 2.The outer surfaces of the piezoelectric layers, and all the four edges of the plate are grounded. Two sets of electric boundary conditions are considered for the inner surfaces of the PZT-4 layers: a close circuit condition with $\phi = 0$ and an open circuit condition with zero electric charge. Since no equipotential condition has been imposed in Ref. [23] on the piezoelectric surfaces under an open circuit condition, the induced electric potential will be nonuniform over the surfaces. This is modelled by associating each element with a separate electric node.

The natural frequency parameter $\bar{f}_n = \omega_n \rho^{1/2} a^2/(2 \times 10^3 \pi h)$ [Hz(kg/m)$^{1/2}$] for the first six modes, predicted by the present IZIGT FE with different mesh sizes, is compared in Table 3 with the 3D exact piezoelasticity solution of Heyliger and Saravanos [23], the ZIGT FE solution of Topdar et al. [31], the DLT FE solutions presented by Saravanos et al. [15] and Robaldo et al. [32] and Murakami-type first- and third-order ZIGT solutions [32]. The results based on the ITOT FE are also listed for comparison. The results are presented for two values of S: 4 and 50, with $a = 1$ m. For simply supported plates, the flexural modes take the form $w_0 = w_0^{mn} \sin(m\pi x/a) \sin(n\pi y/b)$. The values of (m, n) corresponding to the flexural modes are shown in Table 3. The second mode for $S = 4$ is found to be an inplane shear mode, whereas for $S = 50$, all the six modes are flexural ones. The four-node rectangular element of Topdar et al. [31] has 32 mechanical dof per element. The DLT FE results of Saravanos et al. [15] were presented with an 8×8 mesh considering 7 and 20 discrete layers across the laminate thickness. The results of Robaldo et al. [32] are presented with nine-node elements with a 4×4 mesh. For $S = 50$, the results are also compared with the available FSDT FE solution obtained using eight- [18] and nine-node [22] elements. Heyliger and Saravanos [23] presented exact 3D results only for the fundamental flexural frequency. The exact 3D results for frequencies of other flexural modes have been obtained here using the computer program developed in Ref. [24]. The mode number (m, n) is arranged as per the exact 3D solution. Similar results for an open circuit condition are presented in Table 4 for $S = 50$. It is observed that the 3D solution of Heyliger and Saravanos [23] for the fundamental frequency $\bar{f}_1$ matches very well with the present 3D results for the open circuit condition, but differs for the close circuit condition. However, for the close circuit condition, the present 3D results are in excellent agreement with the DLT FE results presented by the same researchers [15]. Also, the predicted difference between the two electric boundary conditions for the DLT results (and also for the present IZIGT results) is consistent with the present exact 3D results, whereas the difference is much smaller in Ref. [23]. This anomaly was duly noted by Saravanos et al.

Table 3
Natural frequencies $\bar{f}_n$ of a square hybrid composite plate under a close circuit condition

S		$\bar{f}_1$	$\bar{f}_2$	$\bar{f}_3$	$\bar{f}_4$	$\bar{f}_5$	$\bar{f}_6$
4	Flexure mode no. (m,n)	(1, 1)	ISM	(1, 2)	(2, 1)	(2, 2)	(1, 3)
	3D exact (H & S [23])	145.339	–	–	–	–	–
	3D exact [24]	141.460	–	253.63	263.89	343.25	383.29
	IZIGT analytical [30]	141.225	–	253.32	263.91	343.60	383.75
	Present IZIGT FE (8 × 8)	140.683	207.66	252.36	263.22	342.50	385.72
	Present IZIGT FE (12 × 12)	140.977	206.92	252.77	263.51	342.53	383.75
	Present IZIGT FE (16 × 16)	141.083	206.66	252.98	263.66	342.87	383.57
	Present TOT FE (16 × 16)	145.332	206.66	265.35	271.35	357.65	408.18
	ZIGT FE [31](8 × 8)	142.86	207.66	256.24	267.04	352.70	390.38
	ZIGT FE [31] (12 × 12)	142.78	206.92	255.48	266.09	348.21	386.90
	ZIGT FE [31] (16 × 16)	142.76	206.67	255.23	265.79	346.81	385.90
	DLT (w-constant) [15][a]	142.469	–	–	–	–	–
	DLT (w-constant) [15][b]	142.221	–	–	–	–	–
	DLT (w-variable) [15][a]	142.942	–	–	–	–	–
	DLT (w-variable) [15][b]	142.630	–	–	–	–	–
	DLT (w-variable) [32]	145.905	–	–	–	–	–
	ZIGT (Murakami—first order) [32]	161.067	–	–	–	–	–
	ZIGT (Murakami—third order) [32]	146.939	–	–	–	–	–
50	Flexure mode no. (m,n)	(1, 1)	(1, 2)	(2, 1)	(2, 2)	(1, 3)	(3, 1)
	3D exact (H & S [23])	245.941	–	–	–	–	–
	3D exact [24]	232.458	523.07	663.40	913.67	1019.6	1366.0
	IZIGT analytical [30]	232.456	523.01	663.57	913.66	1019.4	1366.9
	Present IZIGT FE (8 × 8)	231.513	519.69	660.20	900.05	1014.0	1361.5
	Present IZIGT FE (12 × 12)	232.032	521.45	661.98	907.20	1016.4	1363.9
	Present IZIGT FE (16 × 16)	232.217	522.12	662.66	909.95	1017.6	1365.1
	Present TOT FE (16 × 16)	232.340	522.74	663.73	911.81	1020.0	1369.7
	ZIGT FE [31] (8 × 8)	237.76	537.40	674.83	934.08	1048.6	1388.6
	ZIGT FE [31] (12 × 12)	237.76	537.33	674.72	933.95	1047.7	1387.2
	ZIGT FE [31] (16 × 16)	237.76	537.32	674.70	933.93	1047.6	1387.0
	DLT (w-constant) [15][a]	236.785	–	–	–	–	–
	DLT (w-constant) [15][b]	236.784	–	–	–	–	–
	DLT (w-variable) [15][a]	237.383	–	–	–	–	–
	DLT (w-variable) [15][b]	237.109	–	–	–	–	–
	DLT (w-variable) [32]	248.912	–	–	–	–	–
	ZIGT (Murakami—first order) [32]	276.374	–	–	–	–	–
	ZIGT (Murakami—third order) [32]	248.677	–	–	–	–	–
	FSDT FE (9 node) [22]	206.304	519.444	663.336	907.636	1020.10	–
	FSDT FE (8 node) [18]	246.815	563.075	700.050	979.075	1105.95	–

ISM—inplane shear mode; H & S—Heyliger and Saravanos.
[a]7 layers.
[b]20 layers.

[15], which could not be explained then. It is now clear that their 3D results for close circuit frequencies are erroneous. Therefore, the present 3D results for frequencies are used as benchmarks.

The comparison of the present IZIGT FE results with other available elements reveals that the present DKIZIGT element yields the most accurate results with a maximum error of only 0.6% with respect to the 3D solution for a 16 × 16 mesh, for all flexural modes. The corresponding maximum error in the ITOT FE is 6.5%. The first-order Murakami-type ZIGT is the least accurate with an error of up to 18.9% for the fundamental frequency, $\bar{f}_1$. The present element is also the most computationally efficient among all with only 28 mechanical dof per element. To compare the relative performance of the present element with the 32-dof rectangular element of Ref. [31], which is based on the third-order zigzag theory, analytical (ana.) solutions for the IZIGT of Kapuria and Achary [30] are also listed in Tables 3 and 4. The latter IZIGT is based on a sublayerwise linear description of ϕ across the thickness, and converged results are obtained with 4 sublayers

Table 4
Natural frequencies $\bar{f}_{mn}$ of a square hybrid composite plate under an open circuit condition ($S = 50$)

	$\bar{f}_1$	$\bar{f}_2$	$\bar{f}_3$	$\bar{f}_4$	$\bar{f}_5$	$\bar{f}_6$
Flexure mode no. (m,n)	(1.1)	(1.2)	(2.1)	(2.2)	(1.3)	(3.1)
3D exact (H & S [23])	245.942	–	–	–	–	–
3D exact [24]	245.941	559.41	691.74	965.20	1091.0	1416.9
IZIGT analytical [30]	245.935	559.35	691.87	965.14	1090.8	1417.7
Present IZIGT FE (8 × 8)	244.565	553.33	686.43	945.29	1075.5	1405.6
Present IZIGT FE (12 × 12)	245.320	556.56	689.34	955.82	1083.2	1411.5
Present IZIGT FE (16 × 16)	245.588	557.76	690.43	959.80	1086.4	1414.0
Present TOT FE (16 × 16)	245.734	558.55	691.61	961.98	1089.4	1419.0
DLT (w-constant) [15][a]	259.103	–	–	–	–	–
DLT (w-constant) [15][b]	259.102	–	–	–	–	–
DLT (w-variable) [15][a]	259.630	–	–	–	–	–
DLT (w-variable) [15][b]	259.895	–	–	–	–	–
FSDT FE (9 node) [22]	245.349	558.988	694.196	962.017	1093.006	–
FSDT FE (8 node) [18]	246.912	563.600	700.900	980.725	1108.125	–

[a]7 layers.
[b]20 layers.

in each piezoelectric layer and 2 sublayers in each elastic layer. It can be observed from Table 3 that the present DKIZIGT element with an 8 × 8 mesh (567 mechanical dof) yields more accurate results with respect to the analytical solution than the rectangular element with even a 16 × 16 mesh (2312 mechanical dof), the maximum error for the first six frequencies being 1.5% and 2.8%, respectively, for the two elements, for $S = 50$. With the 16 × 16 mesh, the DKIZIGT element predicts the frequencies with a maximum error of only 0.4% with respect to the analytical solution.

5.2. Convergence study with DKQ and IDKQ interpolation functions

In order to compare the convergence behavior of the present DKIZIGT element with DKQ and IDKQ interpolation functions, the simply supported hybrid composite plate discussed in the previous section is considered. The plate is modelled with varying mesh size $N \times N$. The error in the IZIGT FE results for natural frequencies is computed with reference to the analytical solution of IZIGT of Ref. [30]. The percent error of the predicted natural frequencies ω_n for the first three modes is plotted in Fig. 4 against the mesh size N for thick and thin plates with $S = 4$ and 50, respectively. It is observed that the IDKQ interpolation yields faster convergence and gives more accurate results than the DKQ interpolation for the same mesh size. Similar behavior has been observed for the ITOT-based element too. Therefore, in all previous and subsequent problems, the results are presented with the IDKQ interpolation of w_0, and the DKIZIGT element refers to the IZIGT-based element with IDKQ interpolation functions.

5.3. Other plate configurations for the present study

The accuracy of the present quadrilateral elements for improved ZIGT and TOT based on the IDKQ interpolation of w_0 is also assessed for a hybrid test composite plate (a) with plies of highly inhomogeneous stiffness in tension and shear, and a hybrid soft-core sandwich plate (b), which were analyzed by Kapuria and Achary [30]. Both the hybrid laminates have two PZT-5A layers, each of thickness $0.1h$, bonded to the top and bottom of their elastic substrate. The interfaces of the piezoelectric layers and the substrate are grounded. The outer surface of the top piezoelectric layer is grounded and that of the bottom piezoelectric layer is in the open circuit condition. The substrate of plate (a) has six plies of thickness $(0.08h, 0.12h, 0.2h, 0.2h, 0.12h, 0.08h)$ of materials (2/4/3/3/4/2) with orientations $(0^\circ/0^\circ/90^\circ/0^\circ/0^\circ/0^\circ)$. The substrate of plate (b) is a five-layer sandwich laminate ($0^\circ/90^\circ$/Core/$90^\circ/0^\circ$) with graphite-epoxy faces ($0^\circ/90^\circ$) of material 5 and a soft core of material 6. The thickness of each ply of the face sheet is $0.04h$ and that of the core is $0.64h$.

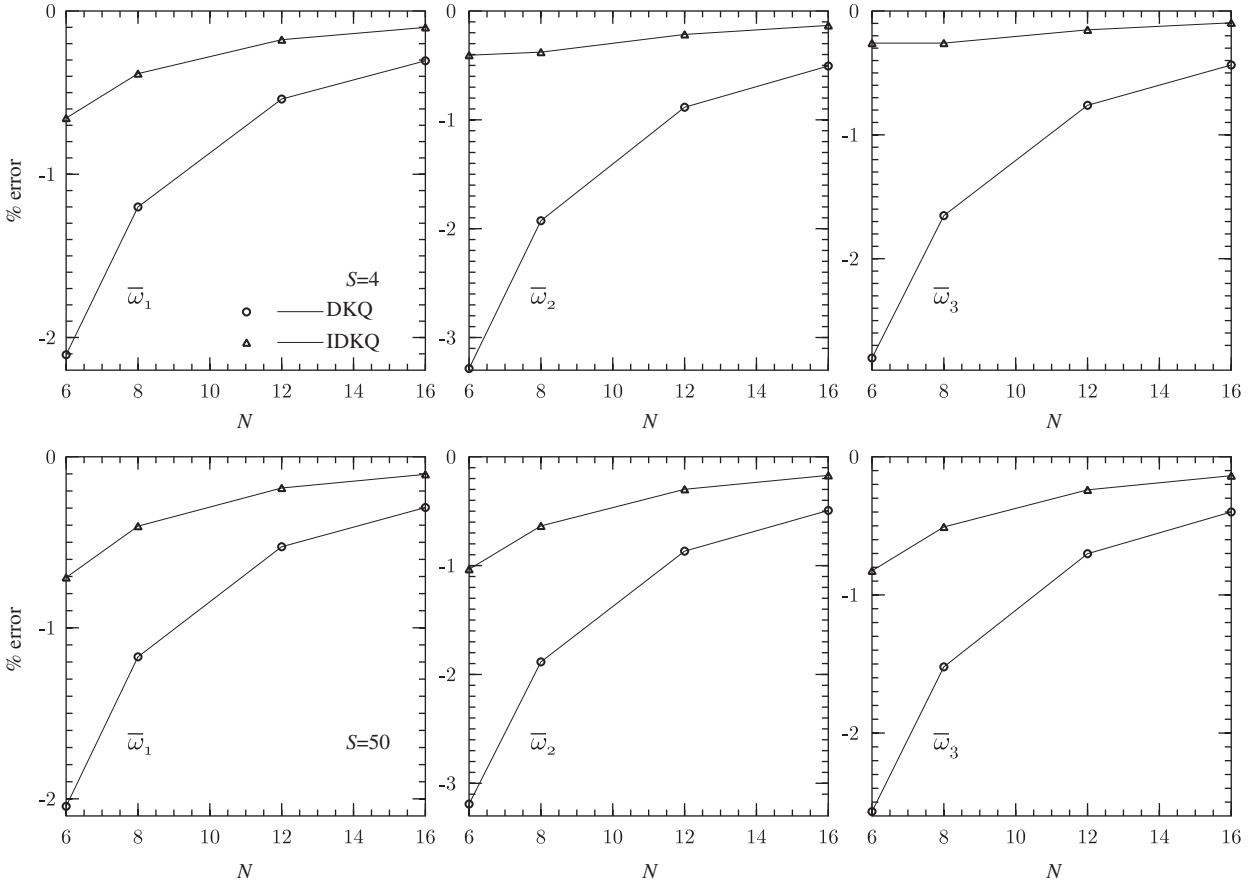

Fig. 4. Convergence study with DKQ and IDKQ interpolations for a square hybrid composite plate.

The circular frequencies ω_n are nondimensionalized as $\bar{\omega}_n = \omega_n a S(\rho_0/Y_0)^{1/2}$ with $Y_0 = 6.9\,\text{GPa}$, and $\rho_0 = 1578\,\text{kg/m}^3$ for plate (a) and $\rho_0 = 1000\,\text{kg/m}^3$ for plate (b). For all round simply supported plates, $\bar{\omega}_n$ is redesignated as $\bar{\omega}_{mn}$ referring to the Fourier mode (m,n) for the purpose of comparison with the analytical solution.

5.4. Hybrid test composite plate

The natural frequencies for flexural modes of a square simply supported hybrid test plate (a) with layers of highly inhomogeneous stiffness are obtained using mesh sizes $N \times N = 6 \times 6$, 8×8, 12×12 and 16×16, for four values of S: 5, 10, 20 and 1000. The IZIGT FE results are compared in Table 5 with the IZIGT analytical solution [30], the exact 3D piezoelasticity solution [30] and the TOT FE results obtained with a 16×16 mesh. The present IZIGT FE results with an 8×8 and finer mesh match very well with the analytical IZIGT solution for all cases, with the error lying in the range of 0.01–0.5% for the 16×16 mesh. The excellent match of the present FE results with the analytical solution for the extremely thin plate with $S = 1000$ establishes that the present elements based on the IZIGT and ITOT are free from shear locking. In comparison with the 3D exact solution, the DKIZIGT element with the 16×16 mesh predicts the fundamental natural frequency $\bar{\omega}_{11}$ with an error of only 0.5%, 0.15% and 0.02% for $S = 5, 10$ and 20, respectively. The corresponding error for the ITOT for this highly inhomogeneous plate is 42.4%, 15.5% and 4.4%, respectively. For the higher modes, the error in the IZIGT predictions is within 1.7% for a moderately thick plate with $S = 10$, whereas the corresponding error for the ITOT is as high as 52.5%. Even for a thinner laminate with $S = 20$, the maximum error in the higher mode frequencies is very large (23.0%) for the ITOT, which is only 0.7% for the

Table 5
Natural frequencies $\bar{\omega}_{mn}$ of a square hybrid test plate (a)

S	Entity	Exact 3D [30]	IZIGT ana. [30]	IZIGT FE				ITOT FE
				6×6	8×8	12×12	16×16	16×16
5	$\bar{\omega}_{11}$	7.4148	7.4489	7.4094	7.4290	7.4439	7.4493	10.555
	$\bar{\omega}_{21}$	14.714	15.169	15.224	15.181	15.165	15.162	24.634
	$\bar{\omega}_{22}$	18.643	19.210	19.418	19.256	19.222	19.225	33.106
	$\bar{\omega}_{31}$	23.621	26.030	27.260	26.590	26.215	26.103	42.175
10	$\bar{\omega}_{11}$	10.034	10.055	9.9834	10.016	10.040	10.049	11.593
	$\bar{\omega}_{21}$	22.397	22.585	22.431	22.489	22.543	22.564	30.286
	$\bar{\omega}_{22}$	29.659	29.796	29.275	29.449	29.638	29.716	42.087
	$\bar{\omega}_{31}$	37.741	38.364	38.783	38.485	38.384	38.368	57.559
20	$\bar{\omega}_{11}$	11.418	11.427	11.339	11.377	11.406	11.416	11.920
	$\bar{\omega}_{21}$	29.024	29.169	28.887	28.999	29.093	29.129	32.620
	$\bar{\omega}_{22}$	40.137	40.221	39.203	39.594	39.933	40.064	46.218
	$\bar{\omega}_{31}$	53.580	54.041	53.862	53.832	53.923	53.975	65.881
1000	$\bar{\omega}_{11}$	12.050	12.050	11.954	11.995	12.025	12.036	12.036
	$\bar{\omega}_{21}$	33.615	33.615	33.259	33.399	33.514	33.558	33.559
	$\bar{\omega}_{22}$	48.198	48.197	46.867	47.382	47.813	47.977	47.980
	$\bar{\omega}_{31}$	69.932	69.932	69.351	69.499	69.704	69.796	69.805

Table 6
Natural frequencies $\bar{\omega}_{mn}$ of a simply supported square hybrid sandwich plate (b)

S	Entity	Exact 3D [30]	IZIGT ana. [30]	IZIGT FE				ITOT FE
				6×6	8×8	12×12	16×16	16×16
5	$\bar{\omega}_{11}$	4.5233	4.5260	4.5081	4.5156	4.5221	4.5245	5.5685
	$\bar{\omega}_{21}$	7.8958	7.9455	8.0375	7.9795	7.9572	7.9529	9.7324
	$\bar{\omega}_{22}$	10.292	10.436	11.044	10.662	10.503	10.470	12.624
	$\bar{\omega}_{31}$	11.950	12.144	13.042	12.503	12.267	12.209	14.474
10	$\bar{\omega}_{11}$	7.3390	7.3302	7.2768	7.3000	7.3175	7.3237	8.4284
	$\bar{\omega}_{21}$	13.880	13.887	13.795	13.818	13.847	13.860	16.656
	$\bar{\omega}_{22}$	18.010	17.918	18.034	17.987	18.032	18.062	22.213
	$\bar{\omega}_{31}$	21.236	21.265	21.614	21.347	21.275	21.270	26.005
20	$\bar{\omega}_{11}$	9.7440	9.7372	9.6566	9.6913	9.7171	9.7263	10.318
	$\bar{\omega}_{21}$	21.357	21.333	21.106	21.194	21.270	21.299	23.677
	$\bar{\omega}_{22}$	29.356	29.318	28.629	28.874	29.107	29.200	33.598
	$\bar{\omega}_{31}$	35.693	35.654	35.565	35.500	35.563	35.603	41.312

IZIGT. This confirms the superiority of the IZIGT over the ITOT having the same number of dof and the inapplicability of the latter for hybrid plates with plies of drastically different material properties. It is evident that the large error in the ITOT is essentially due to the absence of layerwise terms in the assumed expansion of the in-plane displacements along the thickness direction.

5.5. *Simply supported hybrid sandwich plate*

A simply supported square soft-core sandwich plate (b) with piezoelectric layers bonded to the top and bottom is analyzed next, to obtain the natural frequencies of four flexural modes $(m,n)=(1,1),(2,1),(2,2)$ and (3,1). The IZIGT FE results for dimensionless circular frequencies $\bar{\omega}_{mn}$ obtained using various mesh sizes

are compared in Table 6 with the exact 3D solution, the IZIGT analytical solution [30] and the ITOT FE results. It is observed that the natural frequencies predicted by the IZIGT FE with a 16×16 mesh are in excellent agreement with the analytical IZIGT solution with a maximum difference of 0.8% for all four modes and three values of S. The IZIGT FE predicts the natural frequencies very accurately in comparison with the exact 3D piezoelasticity solution, even for a thick hybrid sandwich plate with $S = 5$ with a maximum error of 2.2% for the four flexural modes. In contrast, the ITOT gives highly erroneous results for moderately thick and even thinner plates. For a moderately thick plate with $S = 10$, the % error in the FE results obtained with a 16×16 mesh for the frequencies of the first four flexural modes ranges between 14.8% and 23.3% for the ITOT, whereas the corresponding error for the IZIGT is within 0.3%. Even for a thin plate with $S = 20$, the maximum error in the ITOT for the four frequencies is as high as 15.7%.

Table 7
Natural frequencies $\bar{\omega}_n$ of a square hybrid sandwich plate (b) with boundary conditions CSSS and CSCS

Boundary condition	S	Entity	Mode	3D FE	IZIGT FE				ITOT FE
				(ABAQUS)	12×12	16×16	20×20	24×24	24×24
CSSS	5	$\bar{\omega}_1$	Flexure	4.6958	4.7453	4.7339	4.7287	4.7259	5.7792
		$\bar{\omega}_2$	Flexure	7.7854	7.9243	7.8981	7.8863	7.8801	9.6711
		$\bar{\omega}_3$	Flexure	8.2447	8.4636	8.4148	8.3933	8.3821	10.067
		$\bar{\omega}_4$	Inplane shear	10.286	10.317	10.304	10.298	10.295	10.295
		$\bar{\omega}_5$	Flexure	10.556	10.991	10.880	10.834	10.810	12.900
		$\bar{\omega}_6$	Flex-ure	11.896	12.470	12.370	12.328	12.306	14.314
	10	$\bar{\omega}_1$	Flexure	7.7901	7.8327	7.8173	7.8095	7.8050	9.1217
		$\bar{\omega}_2$	Flexure	13.413	13.449	13.437	13.431	13.428	16.556
		$\bar{\omega}_3$	Flexure	14.388	14.564	14.506	14.478	14.462	17.401
		$\bar{\omega}_4$	Flexure	18.434	18.624	18.565	18.537	18.522	22.736
		$\bar{\omega}_5$	Flexure	20.228	20.365	20.323	20.306	20.297	25.459
		$\bar{\omega}_6$	Inplane shear	20.575	20.634	20.608	20.596	20.590	20.590
	20	$\bar{\omega}_1$	Flexure	10.998	11.031	11.019	11.012	11.007	11.925
		$\bar{\omega}_2$	Flexure	20.932	20.919	20.924	20.925	20.924	23.840
		$\bar{\omega}_3$	Flexure	22.892	23.102	23.029	22.988	22.962	26.073
		$\bar{\omega}_4$	Flexure	30.256	30.332	30.314	30.299	30.288	35.134
		$\bar{\omega}_5$	Flexure	33.771	33.727	33.739	33.745	33.747	40.498
		$\bar{\omega}_6$	Flexure	37.003	37.523	37.334	37.236	37.178	43.612
CSCS	5	$\bar{\omega}_1$	Flexure	4.9036	5.0191	4.9889	4.9750	4.9677	6.0238
		$\bar{\omega}_2$	Flexure	7.8832	8.1034	8.0489	8.0242	8.0110	9.7798
		$\bar{\omega}_3$	Flexure	8.6195	9.0389	8.9304	8.8828	8.8578	10.404
		$\bar{\omega}_4$	Inplane shear	10.286	10.317	10.304	10.298	10.295	10.295
		$\bar{\omega}_5$	Flexure	10.847	11.575	11.358	11.265	11.216	13.194
		$\bar{\omega}_6$	Flexure	11.964	12.631	12.496	12.439	12.409	14.389
	10	$\bar{\omega}_1$	Flexure	8.2930	8.4189	8.3748	8.3528	8.3404	9.8758
		$\bar{\omega}_2$	Flexure	13.588	13.716	13.672	13.649	13.637	16.826
		$\bar{\omega}_3$	Flexure	14.885	15.304	15.161	15.092	15.054	18.099
		$\bar{\omega}_4$	Flexure	18.788	19.279	19.108	19.026	18.981	23.223
		$\bar{\omega}_5$	Flexure	20.308	20.541	20.464	20.429	20.410	25.590
		$\bar{\omega}_6$	Inplane shear	20.575	20.634	20.608	20.596	20.590	20.590
	20	$\bar{\omega}_1$	Flexure	12.416	12.553	12.505	12.477	12.461	13.824
		$\bar{\omega}_2$	Flexure	21.471	21.563	21.532	21.513	21.501	24.619
		$\bar{\omega}_3$	Flexure	24.345	24.917	24.716	24.607	24.542	28.381
		$\bar{\omega}_4$	Flexure	31.162	31.631	31.474	31.386	31.331	36.631
		$\bar{\omega}_5$	Flexure	34.000	34.060	34.037	34.024	34.015	40.855
		$\bar{\omega}_6$	Flexure	38.284	39.531	39.076	38.845	38.708	45.803

CSSS: clamped at $x = 0$, simply supported at $x = a$, $y = 0$, b. CSCS: clamped at $x = 0, a$, simply supported at $y = 0, b$.

5.6. Hybrid sandwich plate with non-simply supported boundary conditions

The square hybrid sandwich plate (b) studied above is also analyzed for two sets of non-simply supported boundary conditions, namely, CSSS (one edge clamped and the remaining three simply supported) and CSCS (two opposite edges clamped and the other two simply supported). The present ZIGT FE results for the first six natural frequencies, obtained with 12×12, 16×16, 20×20 and 24×24 meshes for $S = 5, 10$ and 20, are compared in Table 7 with the converged 3D FE results of ABAQUS obtained using 32,000 [40 (length)$\times$ 40

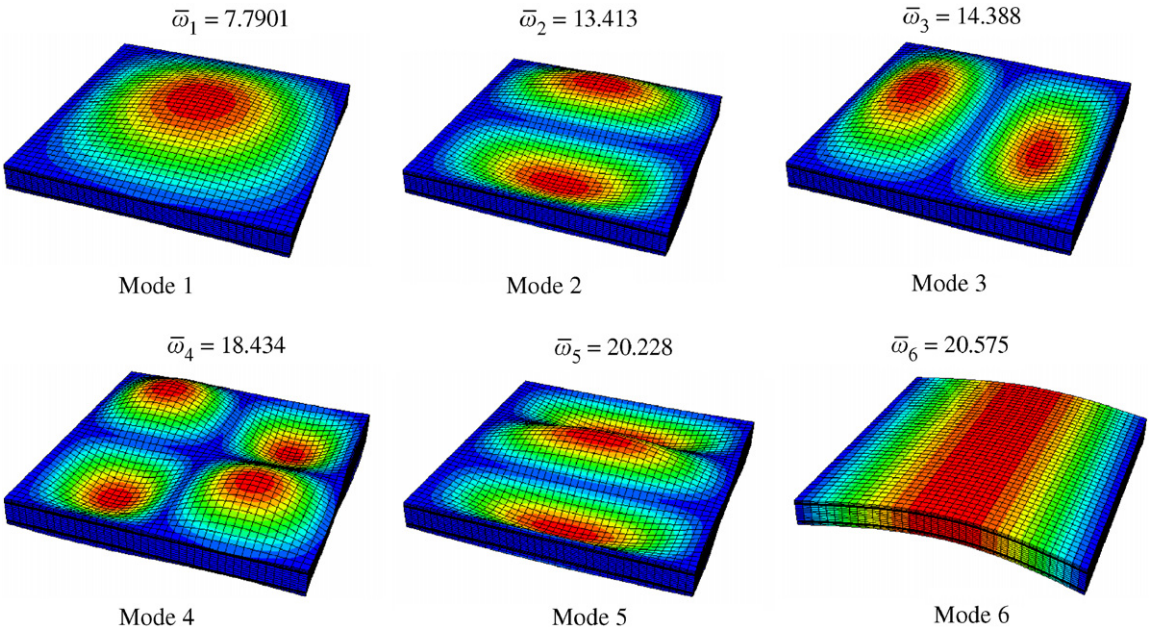

Fig. 5. 3D FE results for the first six mode shapes of a CSSS hybrid sandwich plate (b) with $S = 10$.

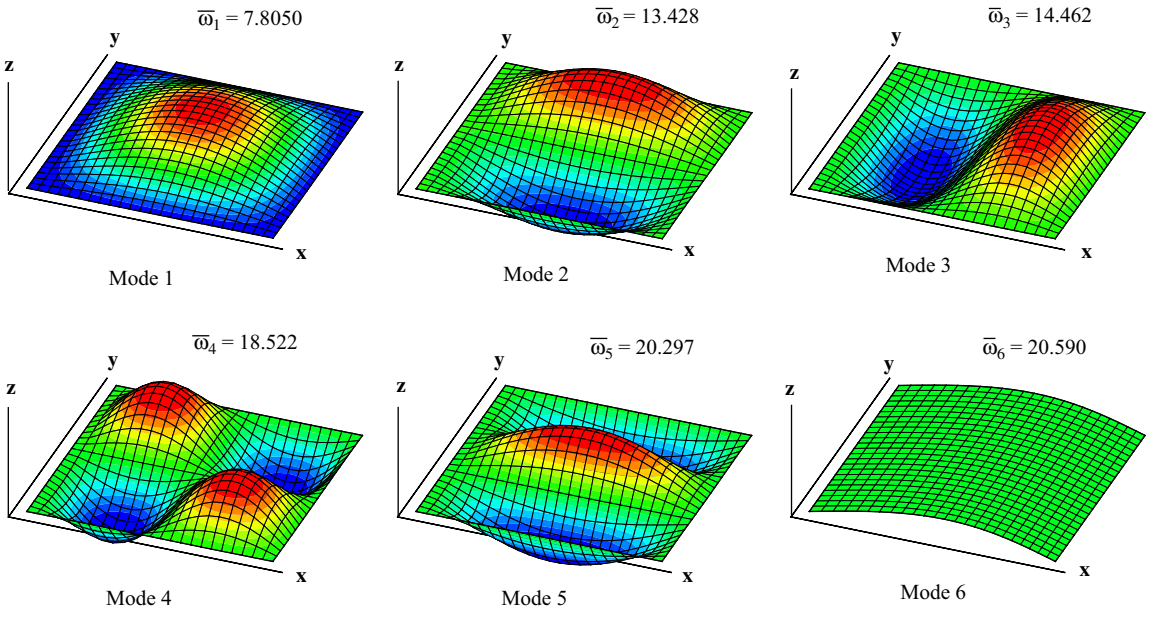

Fig. 6. IZIGT FE results for the first six mode shapes of a CSSS hybrid sandwich plate (b) with $S = 10$.

(width)× 20 (thickness)] 20-node piezoelectric/elastic solid elements. The FE results of ITOT, obtained with a 24×24 mesh, are also presented to assess the accuracy of the ITOT. It is observed that for these boundary conditions too, the present DKIZIGT element predicts the natural frequencies very accurately with respect to the 3D FE solution for all six modes, the maximum percent error for the 24×24 mesh being 3.7, 1.1 and 1.1, respectively, for $S = 5, 10$ and 20. In contrast, the corresponding maximum error for the ITOT is 24.2%, 26.0% and 20.2% for $S = 5, 10$ and 20, respectively. Even for the fundamental frequency of a thin plate with $S = 20$, the error in the ITOT is 11.3% and 8.4% for boundary conditions CSCS and CSSS, respectively. Thus, while the accuracy of the IZIGT for the free vibration response of hybrid sandwich plates with $S \geqslant 5$ is established for all boundary conditions, the ITOT should not be used for free vibration analysis of even thin

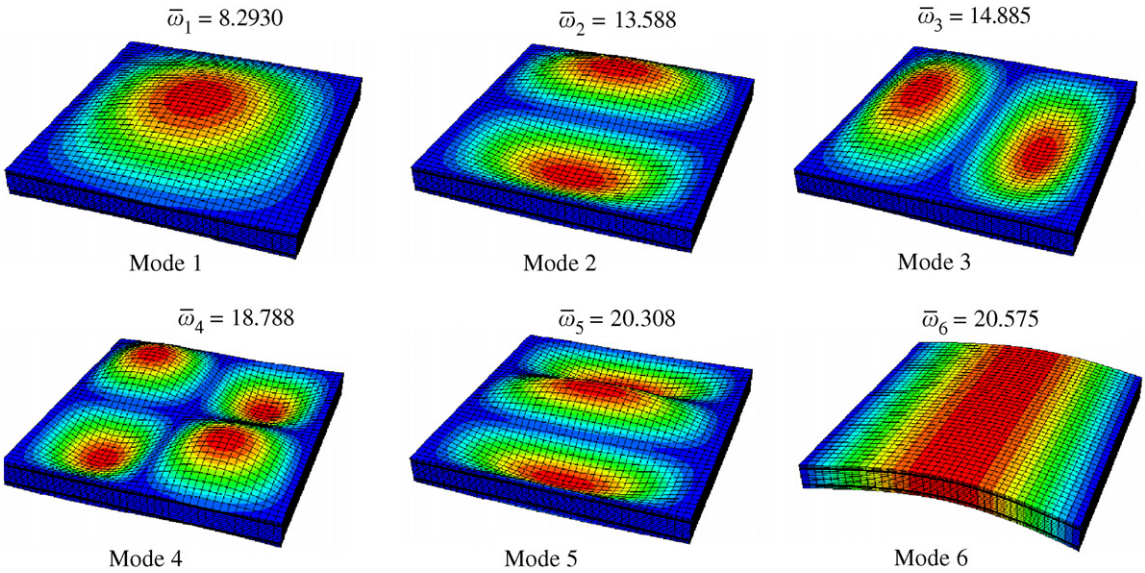

Fig. 7. 3D FE results for the first six mode shapes of a CSCS hybrid sandwich plate (b) with $S = 10$.

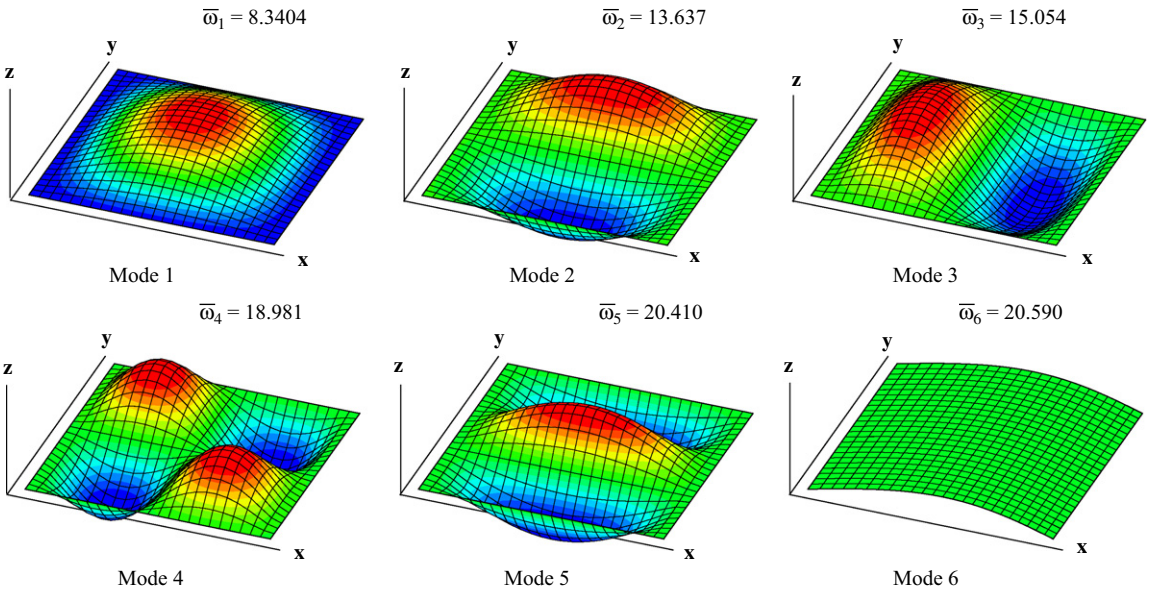

Fig. 8. IZIGT FE results for the first six mode shapes of a CSCS hybrid sandwich plate (b) with $S = 10$.

hybrid sandwich plates with $S = 20$. The mode shapes for the first six modes obtained from the 3D FE analysis and the present IZIGT FE analysis (with 24×24 mesh) for $S = 10$ are shown in Figs. 5 and 6 for the CSSS plate and in Figs. 7 and 8 for the CSCS plate. The comparison shows that the mode shapes predicted by the present IZIGT FE are in excellent agreement with those of 3D FE analysis, for flexural as well as inplane shear modes. It may be seen from Table 7 that the IZIGT and the ITOT give the same results for frequencies of inplane shear modes.

5.7. Skew hybrid plate

In order to assess the performance of the DKIZIGT element for the free vibration response of non-rectangular plates, a skew, cantilever, hybrid sandwich plate (Fig. 9) of laminate configuration (b) is considered with skew angle $\alpha = 30^\circ$ and 45°. The IZIGT FE results for the first six natural frequencies $\bar{\omega}_n$ obtained with different mesh sizes are compared in Table 8 with the converged 3D FE results of ABAQUS obtained with a $40 \times 40 \times 20$ mesh. The results of ITOT FE for the 24×24 mesh are also listed for comparison. As before, the IZIGT FE results are in very good agreement with the 3D FE solution for both

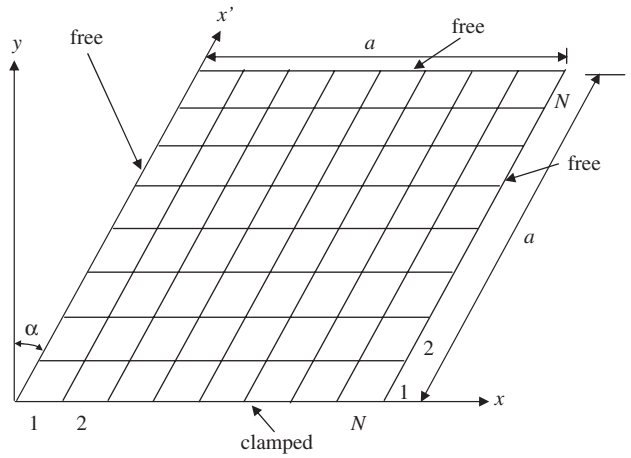

Fig. 9. Geometry of a skew plate with an $(N \times N)$ FE mesh.

Table 8
Natural frequencies $\bar{\omega}_n$ of a cantilever, skew hybrid plate (b) with $S = 10$

Skew angle α	Entity	Mode	3D FE	IZIGT FE				ITOT FE
			(ABAQUS)	12×12	16×16	20×20	24×24	24×24
30°	$\bar{\omega}_1$	Flexure	1.8274	1.8462	1.8410	1.8382	1.8365	1.9757
	$\bar{\omega}_2$	Flexure	3.5752	3.6152	3.6039	3.5980	3.5944	4.0016
	$\bar{\omega}_3$	Flexure	7.5377	7.7271	7.6775	7.6518	7.6366	8.9183
	$\bar{\omega}_4$	Inplane shear	8.1160	8.3266	8.2664	8.2329	8.2120	8.2122
	$\bar{\omega}_5$	Flexure	9.0118	9.0942	9.0750	9.0652	9.0595	10.431
	$\bar{\omega}_6$	Flexure	12.151	12.254	12.230	12.218	12.211	14.115
45°	$\bar{\omega}_1$	Flexure	1.9524	1.9915	1.9811	1.9752	1.9715	2.1271
	$\bar{\omega}_2$	Flexure	4.3844	4.4336	4.4212	4.4144	4.4101	4.9442
	$\bar{\omega}_3$	Inplane shear	7.9729	8.5114	8.3398	8.2475	8.1903	8.1908
	$\bar{\omega}_4$	Flexure	8.1624	8.4903	8.4151	8.3707	8.3424	9.5370
	$\bar{\omega}_5$	Flexure	9.7427	9.8428	9.8219	9.8117	9.8059	11.357
	$\bar{\omega}_6$	Flexure	13.657	13.803	13.773	13.759	13.752	16.215

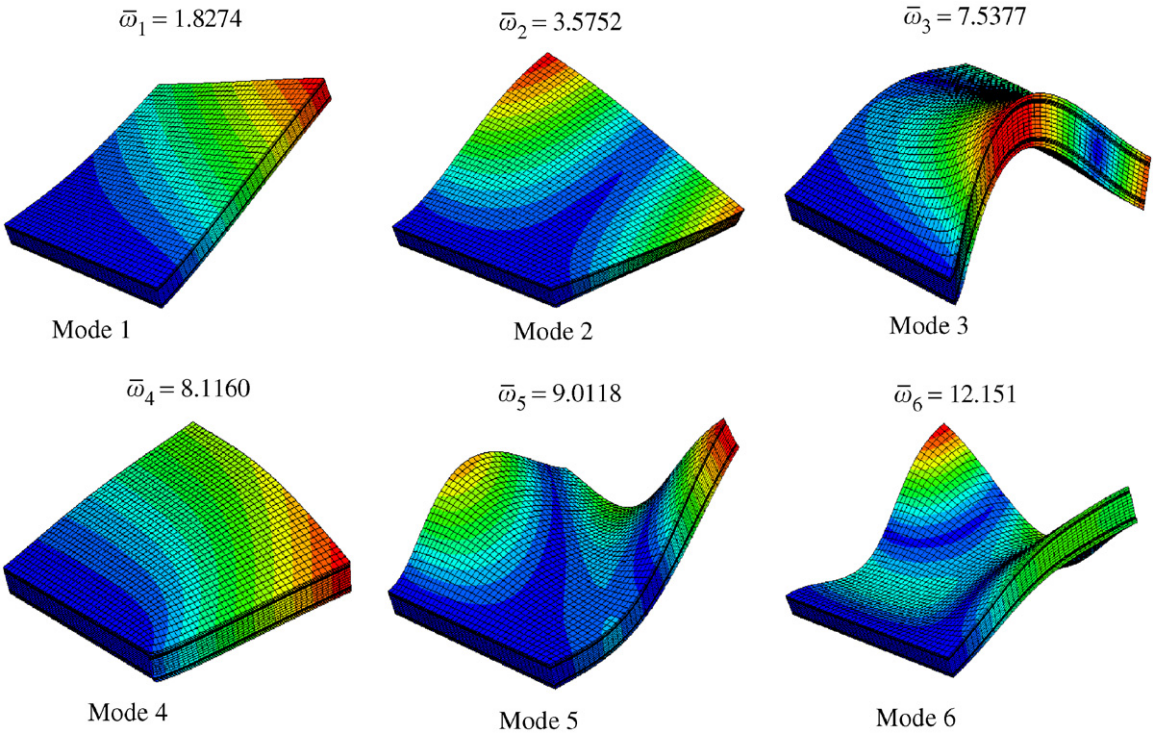

Fig. 10. 3D FE results for the first six mode shapes of a cantilever skew hybrid plate (b) with $\alpha = 30^\circ$.

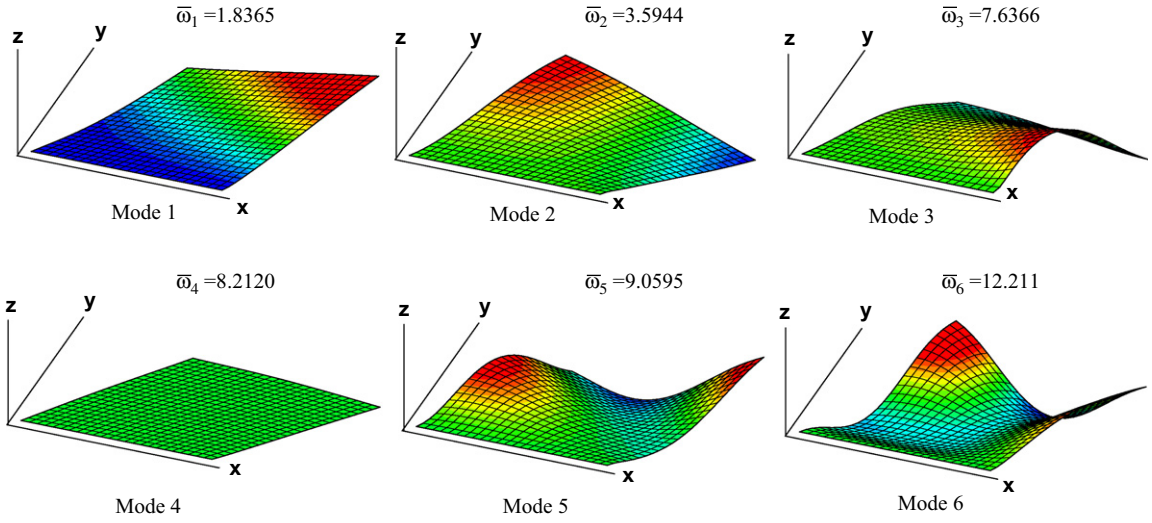

Fig. 11. IZIGT FE results for the first six mode shapes of a cantilever skew hybrid plate (b) with $\alpha = 30^\circ$.

skew angles with a maximum error of 2.2% for the flexural modes, but the ITOT solution is quite erroneous with a maximum error of 18.7%. The mode shapes of the skew plate predicted by the 3D FE and the present IZIGT are plotted in Figs. 10–13 for the six modes for both the skew angles. The present predictions are in excellent agreement with the 3D FE solution. It is observed that modes 3 and 4 become interchanged as the skew angle changes from 30° to 45°.

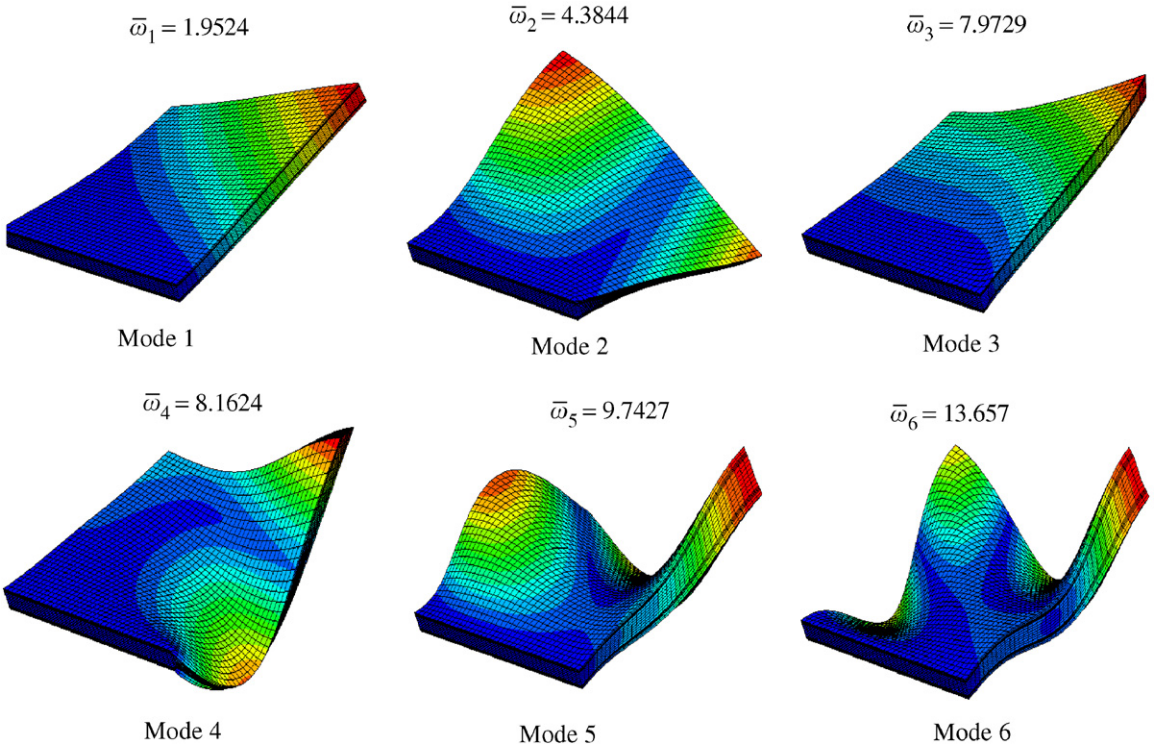

Fig. 12. 3D FE results for the first six mode shapes of a cantilever skew hybrid plate (b) with $\alpha = 45^\circ$.

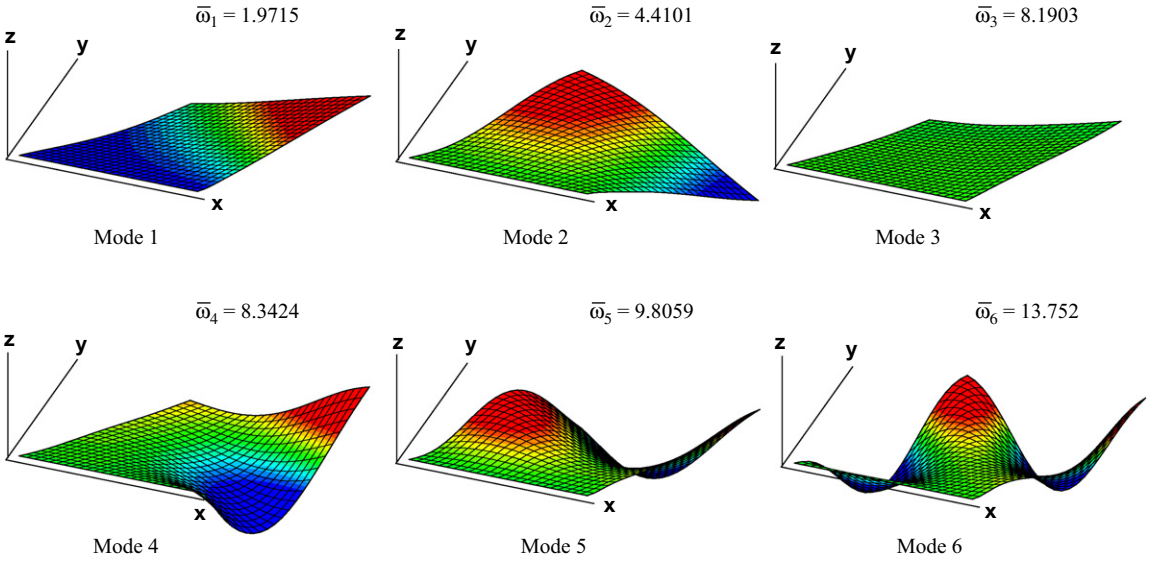

Fig. 13. IZIGT FE results for the first six mode shapes of a cantilever skew hybrid plate (b) with $\alpha = 45^\circ$.

5.8. *Effect of segmentation of the sensor surface*

The free vibration response of a cantilever, rectangular, hybrid sandwich plate (b) with one edge at $x = 0$ clamped and other edges free is obtained for three electric boundary conditions: (i) both top and bottom surfaces grounded (close), (ii) top surface grounded and bottom surface in an open circuit condition

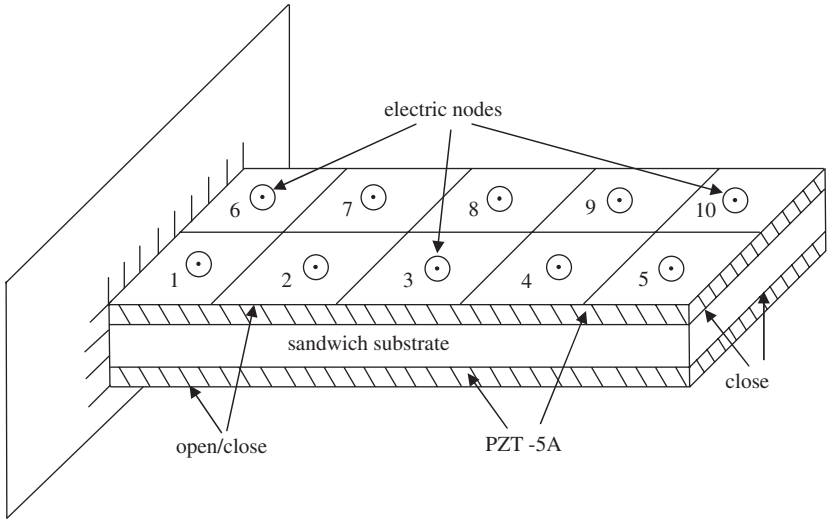

Fig. 14. Hybrid plate (b) with 5×2 electrode segments of the sensor surface.

Table 9
Effect of number of electrodes on $\bar{\omega}_n$ for a cantilever hybrid plate (b)

Condition	Entity	Mode	Number of electrodes				
			1	2×2	5×2	5×4	10×4
Close	$\bar{\omega}_1$	Flexure	1.8156	–	–	–	–
	$\bar{\omega}_2$	Twisting	4.4576	–	–	–	–
	$\bar{\omega}_3$	Extension	5.7086	–	–	–	–
	$\bar{\omega}_4$	Flexure	7.4450	–	–	–	–
	$\bar{\omega}_5$	Twisting	12.685	–	–	–	–
	$\bar{\omega}_6$	Flexure	15.616	–	–	–	–
Open–close	$\bar{\omega}_1$	Flexure	1.8311	1.8400	1.8434	1.8435	1.8443
	$\bar{\omega}_2$	Twisting	4.4576	4.4581	4.4588	4.4589	4.4593
	$\bar{\omega}_3$	Extension	5.7086	5.7535	5.7582	5.7713	5.7724
	$\bar{\omega}_4$	Flexure	7.4646	7.4652	7.4975	7.4976	7.5048
	$\bar{\omega}_5$	Twisting	12.685	12.688	12.695	12.696	12.699
	$\bar{\omega}_6$	Flexure	15.627	15.662	15.688	15.688	15.708
Open	$\bar{\omega}_1$	Flexure	1.8465	1.8648	1.8719	1.8721	1.8737
	$\bar{\omega}_2$	Twisting	4.4576	4.4586	4.4601	4.4602	4.4612
	$\bar{\omega}_3$	Extension	5.7086	5.7987	5.8079	5.8341	5.8363
	$\bar{\omega}_4$	Flexure	7.4848	7.4856	7.5500	7.5502	7.5647
	$\bar{\omega}_5$	Twisting	12.685	12.690	12.706	12.707	12.713
	$\bar{\omega}_6$	Flexure	15.639	15.706	15.759	15.760	15.800

(open-close) and (iii) both top and bottom surfaces in an open circuit condition (open). The plate with $b/a = 0.5$ and $S = 10$ is modelled with a 20×8 mesh. In order to illustrate the effect of segmentation of the electroded sensor surfaces, they are divided into 1, 4 (2×2), 10 (5×2), 20 (5×4) and 40 (10×4) patches of equal size (Fig. 14). This is modelled by assigning an electric node to each electroded pair of patches (at the top and bottom). The dimensionless natural frequencies $\bar{\omega}_n$ for the first six modes for varying number of electrodes are presented in Table 9 for open–close and open conditions. For comparison, the frequencies for the close circuit condition are also listed in the table. It is observed that the natural frequencies increase with the number of surfaces in the open circuit condition and also with the number of equipotential electroded segments in such open circuit surfaces. The open circuit fundamental frequency $\bar{\omega}_1$ with 40 electrodes is larger

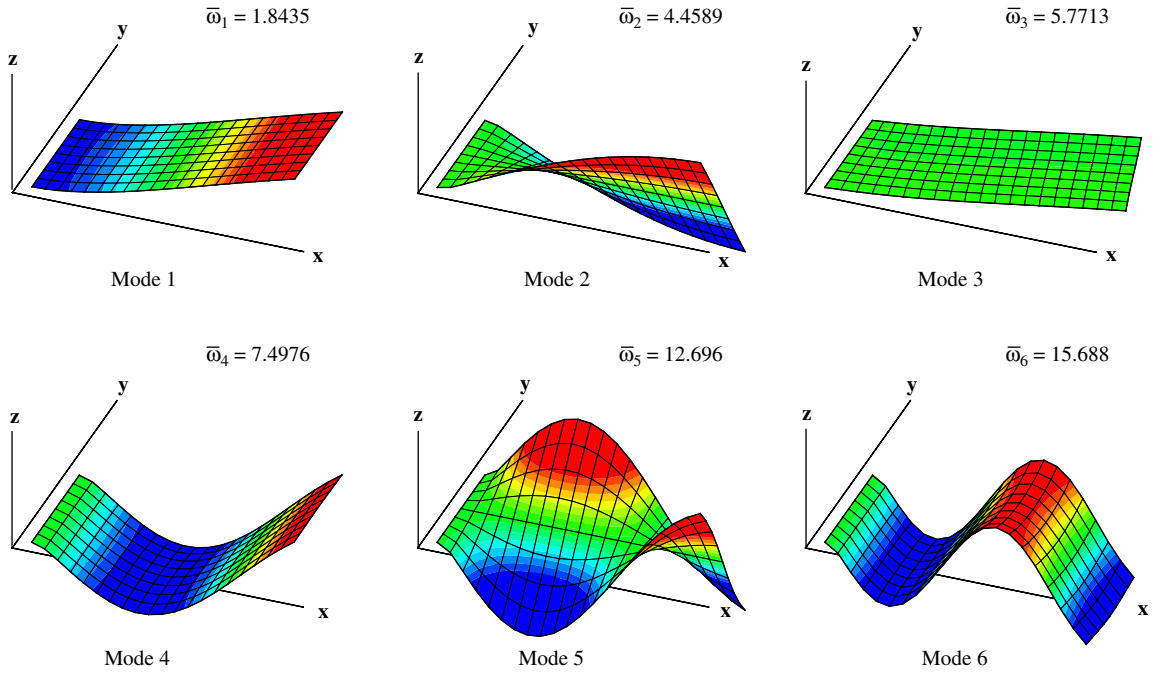

Fig. 15. First six mode shapes for a cantilever hybrid plate (b) with 20 electrodes under an open–close condition.

than the close circuit frequency by 1.6% and 3.2% for open–close and open conditions, respectively. With one electrode, this difference reduces to 0.9% and 1.7% for the above two conditions. As stated earlier, the effective stiffness of the hybrid plate becomes enhanced due to the electromechanical stiffness corresponding to the open circuit potentials Φ_s. Physically, a part of the mechanical energy is converted into electric energy through the induced electric potential and results in an increase in the effective stiffness. Since the degree of constraint of the equipotential condition over the sensory surface decreases with the number of electrode segments, the electromechanical stiffness and consequently the natural frequencies increase with segmentation. The mode shapes of the first six modes of the cantilever hybrid plate with 20 electrode segments, in an open–close condition, are presented in Fig. 15.

6. Conclusions

A novel efficient quadrilateral element with four physical nodes and one electric node is developed based on a coupled improved zigzag theory for dynamic analysis of hybrid composite and sandwich plates. The model considers the equipotential condition of electroded surfaces of piezoelectric layers, and also accounts for the inplane electric field induced by the direct piezoelectric effect. The concept of electric node results in a significant reduction in the number of electric dof. The numerical study reveals that the IDKQ interpolation for the deflection yields faster convergence than the DKQ interpolation for natural frequencies of hybrid plates.

The performance of the element for the free vibration response of hybrid piezoelectric plates has been tested for a variety of plate configurations, namely, piezoelectric bimorph, hybrid cross-ply composite, sandwich and highly inhomogeneous test plates for different boundary conditions and shapes. Comparison of the predicted free vibration response with the 3D piezoelasticity solution and the results of other available 2D theory-based finite elements shows that the present IZIGT-based element is very accurate, robust and computationally efficient. In contrast, the ITOT with the same number of dof yields highly erroneous results for moderately thick plates and even thinner plates with highly inhomogeneous laminates, such as the hybrid sandwich and test plates considered in this study. The number of segments in the electroded surface under an open circuit condition affects the natural frequencies.

The present formulation is readily valid for patch piezoelectric sensors and actuators partly covering the host plate, since it has been formulated based on primary displacement variables in a reference plane, which is taken as the mid-surface of the host-laminated plate. However, numerical implementation of such a general case would require handling elementwise different values of geometry and material parameters, and also variable number of dof per element. These results will be reported in a future study.

References

[1] A. Benjeddou, Advances in piezoelectric finite element modeling of adaptive structural elements: a survey, *Computers and Structures* 76 (2000) 347–363.

[2] J. Mackerle, Smart materials and structures—a finite element approach—an addendum: a bibliography (1997–2002), *Modelling and Simulation in Materials Science and Engineering* 11 (2003) 707–744.

[3] A. Suleman, V.B. Venkayya, A simple finite element formulation for a laminated composite plate with piezoelectric layers, *Journal of Intelligent Material Systems and Structures* 6 (1995) 776–782.

[4] D.T. Detwiler, M.-H.H. Shen, V.B. Venkayya, Finite element analysis of laminated composite structures containing distributed piezoelectric actuators and sensors, *Finite Elements in Analysis and Design* 20 (1995) 87–100.

[5] S.Y. Wang, A finite element model for the static and dynamic analysis of a piezoelectric bimorph, *International Journal of Solids and Structures* 41 (2004) 4075–4096.

[6] V. Balamurugan, S. Narayanan, Shell finite element for smart piezoelectric composite plate/shell structures and its application to the study of active vibration control, *Finite Elements in Analysis and Design* 37 (2001) 713–738.

[7] S.A. Kulkarni, K.M. Bajoria, Finite element modeling of smart plates/shells using higher order shear deformation theory, *Composite Structures* 62 (2003) 41–50.

[8] C.M.A. Vasques, J.D. Rodrigues, Coupled three-layered analysis of smart piezoelectric beams with different electric boundary conditions, *International Journal for Numerical Methods in Engineering* 62 (2005) 1488–1518.

[9] C.M.A. Vasques, J.D. Rodrigues, Active vibration control of smart piezoelectric beams: comparison of classical and optimal feedback control strategies, *Computers and Structures* 84 (2006) 1402–1414.

[10] K.Y. Sze, L.Q. Yao, Modelling smart structures with segmented piezoelectric sensors and actuators, *Journal of Sound and Vibration* 235 (2000) 495–520.

[11] H. Allik, T.J.R. Hughes, Finite element method for piezoelectric vibration, *International Journal for Numerical Methods in Engineering* 2 (1970) 151–157.

[12] H.S. Tzou, C.I. Tseng, Distributed piezoelectric sensor/actuator design for dynamic measurement/control of distributed parameter systems: a piezoelectric finite element approach, *Journal of Sound and Vibration* 138 (1990) 17–34.

[13] S.K. Ha, C. Keilers, F.K. Chang, Finite element analysis of composite structures containing distributed piezoceramic sensors and actuators, *AIAA Journal* 30 (1992) 772–780.

[14] P.R. Heyliger, G. Ramirez, D.A. Saravanos, Coupled discrete-layer finite elements for laminated piezoelectric plates, *Communications in Numerical Methods in Engineering* 10 (1994) 971–981.

[15] D.A. Saravanos, P.R. Heyliger, D.A. Hopkins, Layerwise mechanics and finite element for the dynamic analysis of piezoelectric composite plates, *International Journal of Solids and Structures* 34 (1997) 359–378.

[16] R. Zemcik, R. Rolfes, M. Rose, J. Tessmer, High-performance four-node shell element with piezoelectric coupling for the analysis of smart laminated structures, *International Journal for Numerical Methods in Engineering* 70 (2007) 934–961.

[17] D.A. Saravanos, Passively damped laminated piezoelectric shell structures with integrated electric networks, *AIAA Journal* 38 (2000) 1260–1268.

[18] O. Polit, I. Bruant, Electric potential approximations for an eight node plate finite element, *Computers and Structures* 84 (2006) 1480–1493.

[19] L. Yin, Y. Shen, Strain sensing of composite plates subjected to low velocity impact with distributed piezoelectric sensors: a mixed finite element approach, *Journal of Sound and Vibration* 199 (1997) 17–31.

[20] H. Gu, A. Chattopadhay, J. Li, X. Zhou, A higher order temperature theory for coupled thermo-piezoelectric-mechanical modeling of smart composites, *International Journal of Solids and Structures* 37 (2000) 6479–6497.

[21] J.N. Reddy, A simple higher-order theory for laminated composite plates, *ASME Journal of Applied Mechanics* 51 (1984) 745–752.

[22] V.M.F. Correia, M.A.A. Gomes, A. Suleman, C.M. Mota–Soares, C.A. Mota–Soares, Modelling and design of adaptive composite structures, *Computer Methods in Applied Mechanics and Engineering* 185 (2000) 325–346.

[23] P. Heyliger, D.A. Saravanos, Exact free-vibration analysis of laminated plates with embedded piezoelectric layers, *Journal of Acoustical Society of America* 98 (1995) 1547–1557.

[24] S. Kapuria, G.G.S. Achary, Exact 3D piezoelasticity solution of hybrid cross-ply plates with damping under harmonic electro-mechanical loads, *Journal of Sound and Vibration* 282 (2005) 617–634.

[25] M. Di Sciuva, Multilayered anisotropic plate models with continuous interlaminar stresses, *Composite Structures* 22 (1992) 149–167.

[26] M. Cho, R.R. Parmerter, Efficient higher order composite plate theory for general lamination configurations, *AIAA Journal* 31 (1993) 1299–1306.

[27] E. Carrera, Historical review of zig-zag theories for multilayered plates and shells, *Applied Mechanics Reviews* 56 (2003) 287–308.

[28] S. Kapuria, An efficient coupled theory for multilayered beams with embedded piezoelectric sensory and active layers, *International Journal of Solids and Structures* 38 (2001) 9179–9199.
[29] S. Kapuria, A coupled zigzag third-order theory for hybrid cross-ply plates, *ASME Journal of Applied Mechanics* 71 (2004) 604–614.
[30] S. Kapuria, G.G.S. Achary, A coupled zigzag theory for the dynamics of piezoelectric hybrid cross-ply plates, *Archive of Applied Mechanics* 75 (2005) 42–57.
[31] P. Topdar, A.H. Sheikh, N. Dhang, Vibration characteristics of composite/sandwich laminates with piezoelectric layers using a refined hybrid plate model, *International Journal of Mechanical Sciences* (2007), doi:10.1016/j.ijmecsci.2007.04.001.
[32] A. Robaldo, E. Carrera, A. Benjeddou, A unified formulation for finite element analysis of piezoelectric adaptive plates, *Computers and Structures* 84 (2006) 1494–1505.
[33] K.Y. Sze, X.-M. Yang, H. Fan, Electric assumptions for piezoelectric laminate analysis, *International Journal of Solids and Structures* 41 (2004) 2363–2382.
[34] N.N. Rogacheva, *The Theory of Piezoelectric Shells and Plates*, CRC Press, London, 1994.
[35] M. Krommer, On the correction of the Bernoulli–Euler beam theory for smart piezoelectric beams, *Smart Materials and Structures* 10 (2001) 668–680.
[36] S. Kapuria, S.D. Kulkarni, An improved discrete Kirchhoff quadrilateral element based on third-order zigzag theory for static analysis of composite and sandwich plates, *International Journal for Numerical Methods in Engineering* 69 (2007) 1948–1981.
[37] H.F. Tiersten, *Linear Piezoelectric Plate Vibrations*, Plenum Publishing Corporation, New York, 1969.
[38] S. Kapuria, N. Alam, Efficient layerwise finite element model for dynamic analysis of laminated piezoelectric beams, *Computer Methods in Applied Mechanics and Engineering* 195 (2006) 2742–2760.
[39] O.C. Zienkiewicz, R.L. Taylor, The Finite Element Method, Vol. 2: Solid Mechanics, Butterworth-Heinemann, Oxford, 2000.
[40] C. Jeychandrabose, J. Kirkhope, L. Meekisho, An improved discrete Kirchhoff quadrilateral thin-plate bending element, *International Journal for Numerical Methods in Engineering* 24 (1987) 635–654.
[41] J.L. Batoz, M.B. Tahar, Evaluation of a new quadrilateral thin plate bending element, *International Journal for Numerical Methods in Engineering* 18 (1982) 1655–1677.
[42] T.R. Chandrupatla, A.D. Belegundu, *Introduction to Finite Elements in Engineering*, Pearson Education (Singapore) Pte Ltd., New Delhi, 2002.
[43] M. Petyt, *Introduction to Finite Element Vibration Analysis*, Cambridge University Press, Cambridge, 1990.